A&A 616, A67 (2018)
https://doi.org/10.1051/0004-6361/201732553
© ESO 2018

Astronomy & Astrophysics

Complex cyanides as chemical clocks in hot cores

V. Allen[1,2], F. F. S. van der Tak[1,2], and C. Walsh[3]

[1] Kapteyn Astronomical Institute, University of Groningen, Groningen, The Netherlands
e-mail: allen@astro.rug.nl
[2] SRON, Groningen, The Netherlands
e-mail: vdtak@sron.nl
[3] School of Physics and Astronomy, University of Leeds, Leeds LS2 9JT, UK

Received 26 December 2017 / Accepted 21 March 2018

ABSTRACT

Context. In the high-mass star-forming region G35.20−0.74N, small scale (~800 AU) chemical segregation has been observed in which complex organic molecules containing the CN group are located in a small location (toward continuum peak B3) within an apparently coherently rotating structure.
Aims. We aim to determine the physical origin of the large abundance difference (~4 orders of magnitude) in complex cyanides within G35.20−0.74 B, and we explore variations in age, gas/dust temperature, and gas density.
Methods. We performed gas-grain astrochemical modeling experiments with exponentially increasing (coupled) gas and dust temperature rising from 10 to 500 K at constant H_2 densities of 10^7 cm^{-3}, 10^8 cm^{-3}, and 10^9 cm^{-3}. We tested the effect of varying the initial ice composition, cosmic-ray ionization rate (1.3×10^{-17} s^{-1}, 1×10^{-16} s^{-1}, and 6×10^{-16} s^{-1}), warm-up time (over 50, 200, and 1000 kyr), and initial (10, 15, and 25 K) and final temperatures (300 and 500 K).
Results. Varying the initial ice compositions within the observed and expected ranges does not noticeably affect the modeled abundances indicating that the chemical make-up of hot cores is determined in the warm-up stage. Complex cyanides vinyl and ethyl cyanide (CH_2CHCN and C_2H_5CN, respectively) cannot be produced in abundances (vs. H_2) greater than 5×10^{-10} for CH_2CHCN and 2×10^{-10} for C_2H_5CN with a fast warm-up time (52 kyr), while the lower limit for the observed abundance of C_2H_5CN toward source B3 is 3.4×10^{-10}. Complex cyanide abundances are reduced at higher initial temperatures and increased at higher cosmic-ray ionization rates. Reaction-diffusion competition is necessary to reproduce observed abundances of oxygen-bearing species in our model.
Conclusions. Within the context of this model, reproducing the observed abundances toward G35.20−0.74 Core B3 requires a fast warm-up at a high cosmic-ray ionization rate (~1×10^{-16} s^{-1}) at a high gas density (>10^9 cm^{-3}). The abundances observed at the other positions in G35.20-0.74N also require a fast warm-up but allow lower gas densities (~10^8 cm^{-3}) and cosmic-ray ionization rates (~1×10^{-17} s^{-1}). In general, we find that the abundance of ethyl cyanide in particular is maximized in models with a low initial temperature, a high cosmic-ray ionization rate, a long warm-up time (>200 kyr), and a lower gas density (tested down to 10^7 cm^{-3}). G35.20−0.74 source B3 only needs to be ~2000 years older than B1/B2 for the observed chemical difference to be present, which maintains the possibility that G35.20−0.74 B contains a Keplerian disk.

Key words. stars: massive – astrochemistry – ISM: individual objects: G35.20−0.74N – ISM: molecules

1. Introduction

In high-mass star formation, the hot molecular core (HMC) stage is marked by high abundances of complex organic molecules (COMs), molecular species containing at least six atoms including carbon and hydrogen (Herbst & van Dishoeck 2009), and emitting from a warm (100–500 K), dense ($n_H > 10^7$ cm^{-3}), and compact (<0.05 pc) region. The physical nature of this type of region, whether a disk, an outflow cavity, or an envelope, is currently unknown. The COMs seen in hot cores are expected to be abundantly produced in the ice mantles hosted on dust grains around the forming star and released into the gas phase upon warming. Also, COMs can be produced through endothermic reactions in warm gas. The HMC stage is not expected to last more than 10^5 years, as COMs are dissociated in the expanding HII region around a young high-mass star. As a short-lived stage with specific physical parameters, the HMC is an ideal source for studying the process of high-mass star formation and by tracing the distribution of specific molecular species, we can learn more about the physical and chemical structure of these young objects.

Chemical segregation has been observed in several different star-forming regions on scales from 1000 to 8000 AU, most famously in Orion KL where Blake et al. (1987) observed that the hot core has a much higher abundance of N-bearing species than the compact ridge and surrounding sources. To explain this, Caselli et al. (1993) modeled shells of gas collapsing toward the nearby object IRc2, which are halted and heated up showing different chemical compositions (see Feng et al. 2015 and Crockett et al. 2015 for recent work on Orion KL). A difference in chemical composition has also been seen between W3(OH) and W3(H_2O) (Wyrowski et al. 1999) where the latter is a strong N-bearing source with various complex organics, but the former only contains a handful of O-bearing species. AFGL2591 VLA 3 is another source (Jiménez-Serra et al. 2012) where such chemical segregation has been observed on a scale of a few thousand AU, which was explained using models of concentric shells with different temperatures and amounts of extinction.

This paper follows our previous study (Allen et al. 2017) of G35.20-0.74N (G35.20), a high-mass star-forming region containing several high-mass protostars at a distance of 2.19 kpc with a bolometric luminosity of $3.0\times10^4\,L_\odot$

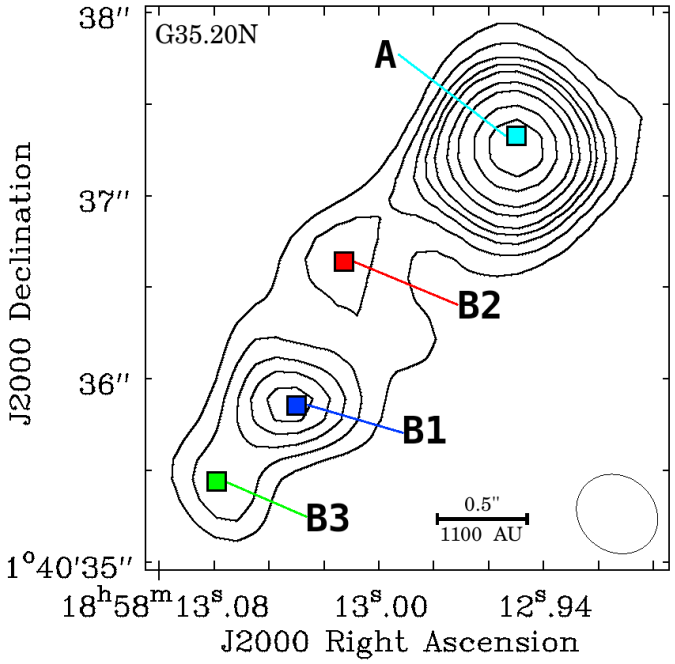

Fig. 1. 870 μm continuum emission from Cycle 0 ALMA observations of G35.20. The continuum peaks are labeled in order of intensity (i.e., peak B1 has the highest and peak B3 the lowest continuum intensity). Contour levels are 0.03, 0.042, 0.055, 0.067, 0.08, 0.10, 0.13, 0.18, and 0.23 Jy beam^{-1} (σ = 1.8 mJy beam^{-1}). The pixel-sized colored squares denote each of the spectral extraction points (from Allen et al. 2017).

(Sánchez-Monge et al. 2014). G35.20 was shown to be a strong Keplerian disk candidate based on position-velocity diagrams for several species and the fit of the velocity field to a Keplerian disk model (Sánchez-Monge et al. 2013). In this source, we observed a segregation in Core B between complex N-bearing species, especially cyanides (those containing the CN group), and other COMs on a scale of less than 1000 AU within an apparently coherent source presenting a potential signature of Keplerian rotation. Within Core B (shown in Fig. 1) there is a higher abundance (generally 1–2 orders of magnitude) of almost all observed species to the southeast (at continuum peak B3), and additionally, the nitrogen-bearing species abundance drops quickly when proceeding to the northwest (to continuum peaks B1 and B2 about 1000 and 2000 AU from source B3, respectively) where most complex N-bearing species (especially those with the CN group) are no longer detected. This is especially prominent in ethyl- and vinyl cyanide (C_2H_5CN and CH_2CHCN) and in vibrationally excited states and isotopologs of methyl cyanide (CH_3CN) and cyanoacetylene (HC_3N). We also model the observed abundances from Core A for comparison, as it is not part of the potential Core B disk system, but has a similar chemical composition to source B3 with high abundances of cyanides and oxygen-bearing species.

We expect G35.20 source B3 to be a high-mass source as a high kinetic temperature is observed toward peak B3 (~300 K) compared to peak B1 and peak B2 (160 and 120 K, respectively). Alongside this high temperature, the deuterium fraction is very high toward source B3 (13% for CH_3CN) implying that it has only recently heated up, releasing deuterium enriched ices into the gas phase. There is also a cluster of OH masers toward peak B3 (Hutawarakorn & Cohen 1999). At the outer radius of this disk candidate, the rotation period is between 9700 and 11 100 years, which is fast enough that such a difference in chemistry should not be present because of the mixing of gas. In this work, we use chemical modeling to investigate a cause for chemical segregation between complex cyanides and other species related to age, temperature, warm-up time, or gas density.

Table 1. Initial ice composition vs. H_2O ice.

Species	IC 1	IC 2	IC 3	IC 4	IC 5
CO (ice)	10%	5%	10%	8%	17%
CO_2 (ice)	10%	15%	10%	13%	23%
NH_3 (ice)	5%	2%	5%	15%	15%
CH_3OH (ice)	5%	5%	5%	10%	4%
HCOOH (ice)	10%	5%	10%	7%	1%
CH_4 (ice)	5%	1%	5%	1.5%	1.5%
H_2CO (ice)	10%	2%	10%	3.5%	2%

Notes. The initial H_2 abundance for all models is 50% of the total material. The H_2O ice abundances vs. the total composition are 5×10^{-6} for IC 1, 5×10^{-5} for IC 3, and 10^{-5} for IC 2, 4, and 5.

2. Chemical model

2.1. Model setup

We used a large gas-grain chemical network (668 species, over 8000 reactions) in which the gas-phase reactions are from the UMIST Database for Astrochemistry (McElroy et al. 2013) known as Rate12[1], and the grain-surface and gas-grain interactions are extracted from the Ohio State University (OSU) network (detailed description in Walsh et al. 2014). Our network includes the following reaction types: two-body gas-phase reactions, direct cosmic-ray ionization, cosmic-ray-induced photoreactions, photoreactions, cation–grain recombination, adsorption onto grains, thermal desorption, photodesorption, grain-surface cosmic-ray-induced photoreactions, grain-surface photoreactions, two-body grain-surface reactions, and reactive desorption.

In this model, the thermal desorption rate depends on the binding energy of the species ($E_{\rm bind,A}$) and the number density of that species on the grain-surface ($n_{\rm s}$(A)). If there are less than two monolayers, then the following first order rate is used: $f_{\rm thermal,A} = k_{\rm evap,A} n_{\rm s}$(A) (Cuppen et al. 2017), where $k_{\rm evap,A} = \nu \exp^{-\frac{E_{\rm bind,A}}{kT}}$ and ν is the characteristic attempt frequency. Once there are more than two monolayers, then the following zeroth-order approximation: $f_{\rm thermal,A} = k_{\rm evap,A} N_{\rm act} \chi_{\rm A} N_{\rm s} \sigma_{\rm g} n_{\rm grain}$, where $N_{\rm act}$ is the number of active monolayers, $\chi_{\rm A}$ is the fractional abundance of species A, and $N_{\rm s}\sigma_{\rm g} n_{\rm grain}$ is the number of available surface sites per unit volume. Further details about this chemical code can be found in Drozdovskaya et al. (2014) and Walsh et al. (2014, 2015). Reaction–diffusion competition is included.

The model considers a single embedded (A_V = 10) point source at a constant gas density that is warming up over time. The relatively high extinction means that the only source of ionization and photodissociation in the model is cosmic rays. A low cosmic-ray ionization rate of 1.3×10^{-17} s^{-1} was used in the fiducial model. Higher cosmic-ray ionization rates are explored in test cases (Sects. 3.2–3.6).

[1] http://www.udfa.net/

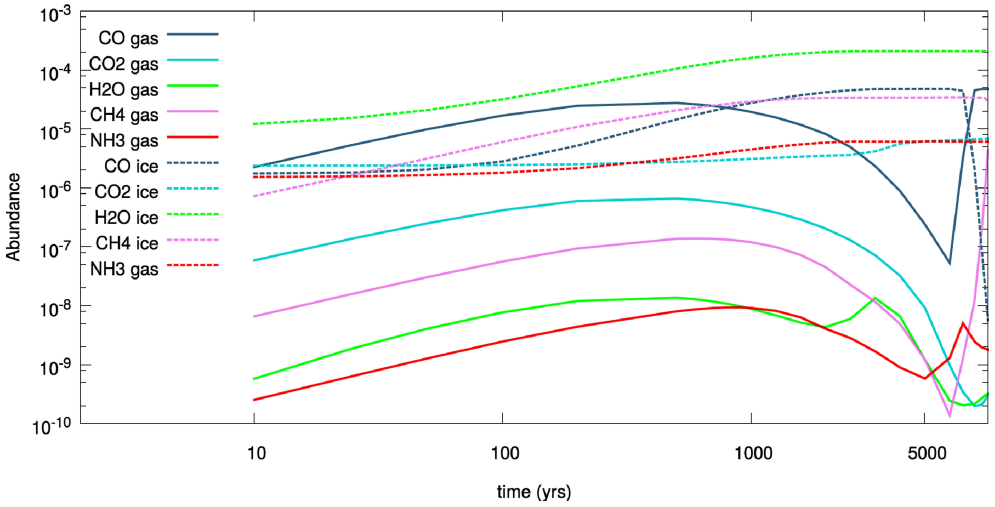

Fig. 2. Abundances of simple species over time for a fast warm-up with a gas density of 10^7 cm^{-3}. Dashed lines show ice abundances and solid lines show gas abundances.

Table 2. Abundances vs. H_2 across G35.20 from Allen et al. (2017).

Species	Source A	Source B1	Source B2	Source B3
CH_3OH	5.0×10^{-7}	6.2×10^{-7}	6.7×10^{-7}	1.4×10^{-6}
C_2H_5OH	3.0×10^{-9}	9.4×10^{-10}	3.1×10^{-10}	5.2×10^{-9}
CH_3CHO	1.1×10^{-9}	1.9×10^{-9}	6.9×10^{-10}	1.7×10^{-9}
CH_3OCHO	3.4×10^{-9}	7.0×10^{-9}	6.1×10^{-9}	1.1×10^{-8}
CH_3CN	3.0×10^{-9}	1.7×10^{-9}	3.9×10^{-10}	3.1×10^{-9}
CH_2CHCN	5.3×10^{-10}	$<1\times10^{-13}$	$<2\times10^{-13}$	3.0×10^{-10}
C_2H_5CN	6.4×10^{-10}	$<7\times10^{-14}$	$<1\times10^{-13}$	5.2×10^{-10}
HC_3N	5.1×10^{-10}	2.4×10^{-10}	5.9×10^{-11}	3.1×10^{-9}

2.2. Initial conditions

We start a warm-up phase at the end of a theoretical collapse phase that results in a constant H_2 density of $n = 10^7$, 10^8, or 10^9 cm^{-3} with enhanced ice abundances of several species (see Table 1). The gas density of Core B is expected to be 10^7–10^8 cm^{-3} and Core A is expected to have a density of 10^9 cm^{-3} from Sánchez-Monge et al. (2014). The warm-up phases start with the initial conditions (IC) outlined in Table 1 and the (coupled) gas and dust temperature increases from 10 to 500 K over 52 (fast), 203 (medium), or 1000 (slow) kyr according to the equation $T(t) = 10 + \kappa t^2$ as based upon the methods in Viti et al. (2004), Garrod & Herbst (2006), and Garrod et al. (2008). The values of κ used in this work to warm from 10 to 500 K in the prescribed times for the fast, medium, and slow warm-ups are 1.96×10^{-22}, 1.2×10^{-23}, and 4.9×10^{-25} K s^{-2}, respectively.

The initial ice abundances for IC 2, 4, and 5 are from ice observations carried out by Gibb et al. (2004) of three high-mass star-forming regions, i.e., AFGL 2136, W33A, and NGC 7538 IRS9, respectively. Initial conditions (IC) 1 and 3 are based on a lower limit of the water abundance of 10^{-5} vs. H_2 and an upper limit of water abundance of 10^{-4} vs. H_2 as suggested in van Dishoeck (2004). Other molecular abundances in IC 1 and 3 are then percentages of 5% (for NH_3, CH_3OH, and CH_4 ice) or 10% (for CO, CO_2, HCOOH, and H_2CO ice) of water. The atomic gas abundances in our model are the result of subtracting the atoms that have gone into molecules from the typical gas abundances found in the pristine model input. Our approach differs from Garrod et al. (2008) in that their model includes a phase of initial collapse from diffuse cloud to dense core, thereby building up their ices in a model-dependent manner. Our full gas and ice initial conditions are detailed in Appendix A. While we did not include molecular gas in our initial abundances, the chemistry quickly converts the free atoms into stable molecules (Fig. 2). These gas-phase abundances are within an order of magnitude of reported abundances in starless and prestellar cores (Ruoskanen et al. 2011; Koumpia et al. 2016; Vastel et al. 2016).

2.3. Modeling approach

First, we tested the fiducial model (Sect. 3.1): three different densities (based on the expected densities of our observed sources) at three different warm-up speeds based on expected gas warming speed around low-, intermediate-, and high-mass stars (discussed in Sect. 4.3) for the five initial conditions outlined above (Sect. 2.2). After the basic test, we tested models that each changed one feature of the fiducial model for a fast warm-up (as expected for a high-mass source). These were, excluding reaction–diffusion competition (Sect. 3.2), changing the initial temperature to 15 or 25 K (Sect. 3.3), running time at a high temperature (300 K) after the warm-up period (Sect. 3.4), adding HCN to the initial ice (Sect. 3.5), and raising the cosmic-ray ionization rate to 1×10^{-16} s^{-1} and 6×10^{-16} s^{-1} (Sect. 3.6). Modeled abundances for each test were compared to the observed abundances from Allen et al. (2017) shown in Table 2 and their associated upper and lower limits to constrain the time period during which all abundances could be reproduced by the model.

3. Results

We aim to constrain the time periods during which the models reasonably reproduce the observed abundances within observed error limits (detailed in Table 2) of the following molecules: cyanides (CH_3CN, CH_2CHCN, C_2H_5CN), cyanoacetylene (HC_3N), methanol (CH_3OH), methyl formate (CH_3OCHO), acetaldehyde (CH_3CHO), and ethanol (C_2H_5OH). For a time period to be an acceptable fit, its duration must be less than half a disk rotation period (<5 kyr). The focus species include all of the cyanides observed in G35.20 and most of the complex organic oxygen-bearing species. The abundances in Table 2 were determined using detailed modeling of ALMA observations of spectral lines from the four continuum points in Fig. 1 (Allen et al. 2017) using the software XCLASS (Möller et al. 2017), assuming local thermal equilibrium (LTE). The key result from this analysis was that continuum peak B3 showed higher abundances of almost all modeled species, but especially of those containing the CN group. Two in particular, vinyl and ethyl cyanide (CH_2CHCN, C_2H_5CN), were not detected at

Table 3. Time ranges (in kyr) that fit observed abundances using the fiducial model in the lower abundance sources, B1/B2, those for the higher abundance source, B3, and the other hot core in this group, A.

Density	Warm-up time	A		B1/B2		B3	
		Time range	Temperature	Time range	Temperature	Time range	Temperature
(cm^{-3})	(kyr)	(kyr)	(K)	(kyr)	(K)	(kyr)	(K)
10^7	52	21.6–28.5	93–158	20.0–25.0	81–123	C_2H_5CN 2 × too low	
10^8	52	22.1–28.5	97–158	22.0–23.3	96–107	C_2H_5CN 3 × too low	
10^9	52	C_2H_5CN 5 × too low		21.5–24.0	92–114	C_2H_5CN 10 × too low	
10^7	203	85.0–97.3	94–121	75.5–90.0	76–105	84.5–97.5	93–116
10^8	203	86.0–105.0	96–139	85.5–91.0	95–107	87.0–115.0	98–165
10^9	203	88.7–103.0	102–134	88.0–94.5	100–114	89.6–103.0	104–134
10^7	1000	365–472	75–119	365–425	75–98	375–475	78–120
10^8	1000	415–490	94–127	410–455	92–111	420–490	96–127
10^9	1000	430–500	100–132	420–460	96–113	435–500	102–132

Notes. Corresponding temperatures are also shown (in K). Full details in Appendix A.

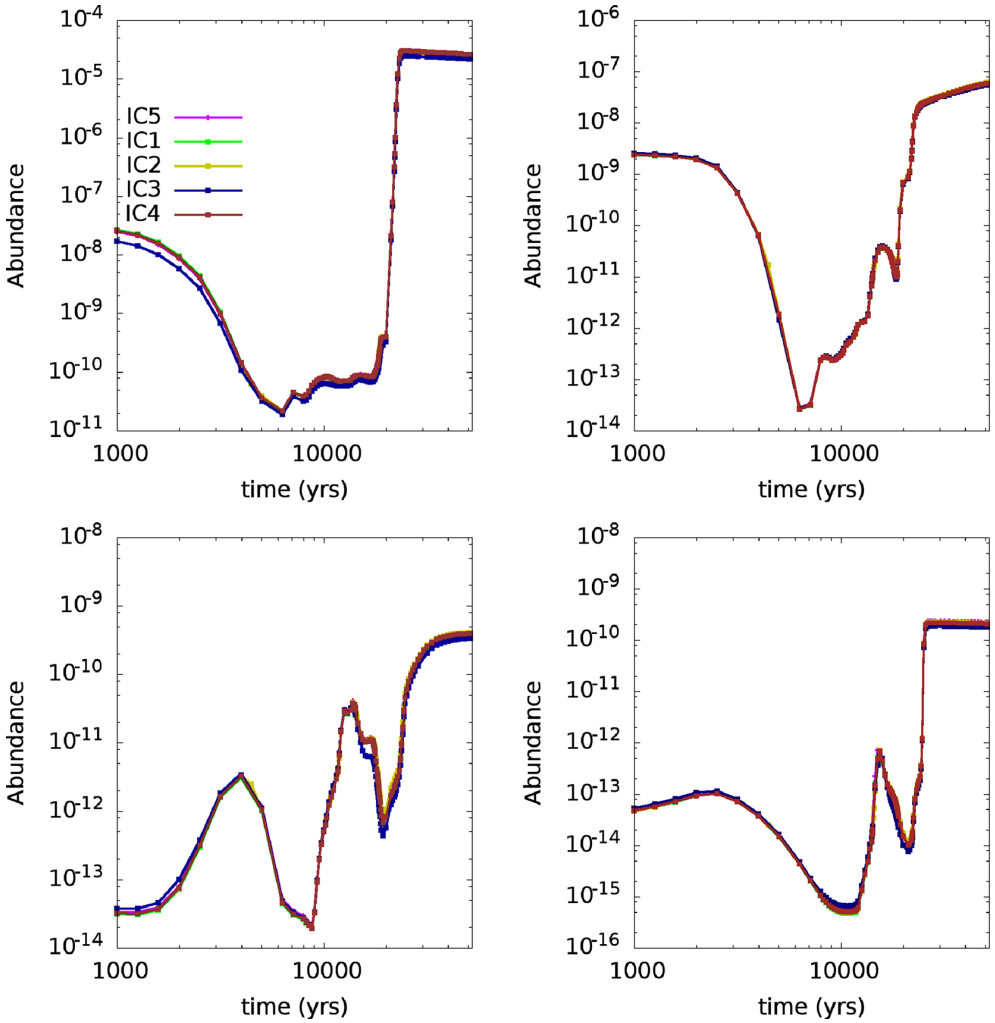

Fig. 3. Fractional abundance vs. H_2 for one species with different initial conditions (ICs 1-5) for a gas density of $10^7\,cm^{-3}$ and a fast warm-up time of 50 kyr. Results are similar for other warm-up times and densities.

continuum peaks B1 and B2, giving an upper limit to their abundances of 1×10^{-13} with respect to H_2. Upper and lower limits for the XCLASS modeling results can be found in Appendix B.

We find little variation among the different starting conditions (see Fig. 3), so in the following analysis we use the initial ice composition of IC5 as NGC 7538 IRS9 has a similar bolometric luminosity and distance to G35.20 ($4 \times 10^4\,L_\odot$ and 2.7 kpc for NGC 7538 IRS9 vs. $3 \times 10^4\,L_\odot$ and 2.2 kpc for G35.20).

3.1. Fiducial model

In our fiducial model, we begin with gas and dust at 10 K and the initial ice and gas conditions of IC5, then warm the gas and dust at fast, medium, and slow speeds (detailed in Sect. 2.1) to 500 K at a constant gas density. All of the tests in the following subsections begin with the conditions of this fiducial model varying one parameter. Time ranges and corresponding gas temperature ranges for all fits are summarized in Table 3.

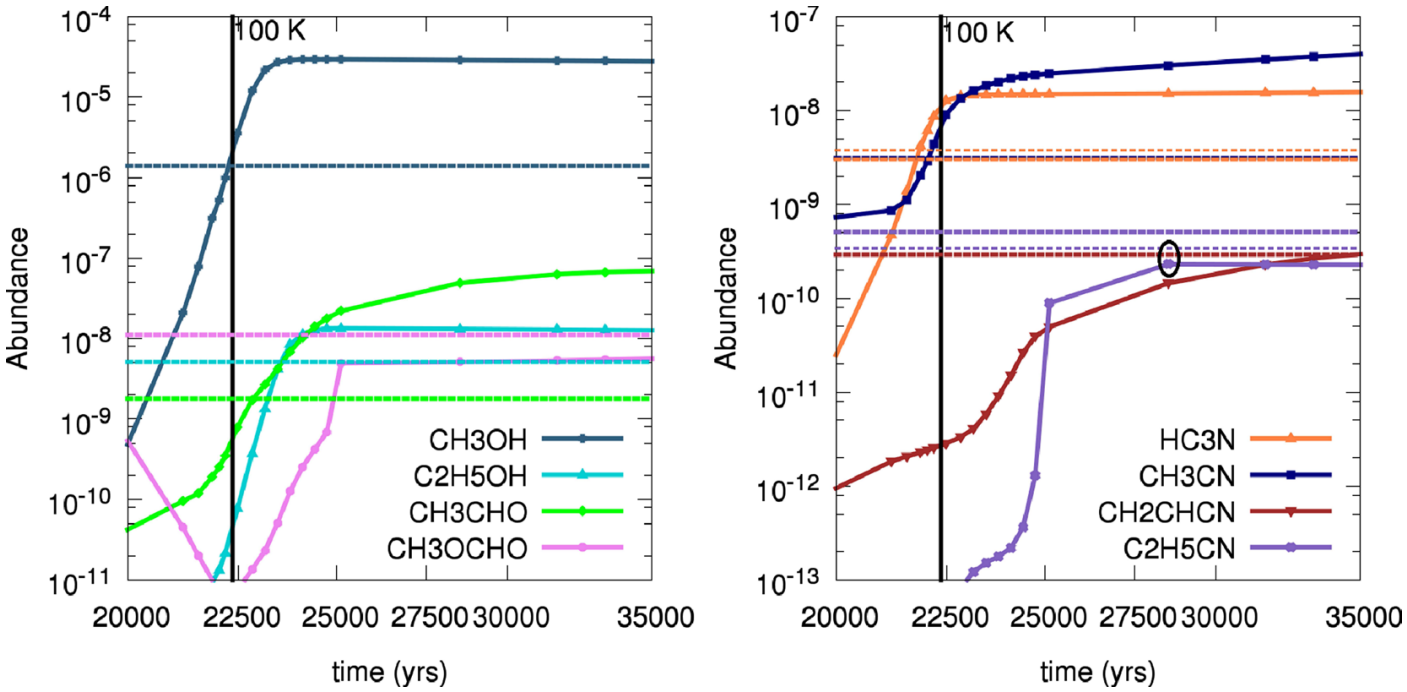

Fig. 4. Fractional abundance for B3 fast warm-up (from 10 to 500 K) model at a density of 10^7 cm^{-3} for the time period 20 000–35 000 yr with the fiducial model. Oxygen-bearing species are shown to the left and nitrogen bearing to the right. The *y*-axes have different scales. All species are shown in the key with color-coded dashed horizontal lines showing the observed abundances for B3. The thinner dashed lines indicate the upper limit for HC_3N and the lower limit for C_2H_5CN, as they are the species that best constrain the time span. The black ellipse highlights the difference between the modeled abundance of C_2H_5CN and the lower limit of the observed abundance. At the higher densities we tested, the model abundance of C_2H_5CN is lower.

Fast warm-up models can reproduce all of the abundances observed for peaks B1/B2 and the C_2H_5CN abundance can be reproduced in core A for densities of $n = 10^7$ and 10^8 cm^{-3}. The model C_2H_5CN abundance at peak B3 cannot be reproduced by the fiducial model, although at a density of 10^7 cm^{-3} it is 1.4×10^{-10} lower (50%) than the minimum observed abundance (see Fig. 4). This difference is significantly larger than the tolerance for the model (10^{-13}) and is therefore not a fit. A summary of the time periods where the observed abundances of HC_3N, CH_3CN, CH_2CHCN, C_2H_5CN, CH_3OCHO, and C_2H_5OH are reproduced in a fast warm-up for all sources and gas densities is shown in Fig. 5.

Medium-speed warm-up models can reproduce the C_2H_5CN abundance observed in source B3 at late times (after 97 kyr). The time period required to reproduce all observed abundances is >13 kyr, which is longer than a disk rotation period. Abundances in source B1/B2 can be reproduced in a medium warm-up in ~5.5 kyr. See Appendix D for tables detailing the times at which observed abundances are replicated by the fiducial model and further plots of abundance over time.

Slow warm-up models for all three densities can reproduce all of the observed abundances. The time periods needed to reproduce the observed abundances are shorter for $n = 10^8$ and 10^9 cm^{-3}, although still very long (>40 kyr). For peaks B1/B2 the shortest time range is 40 kyr at $n = 10^9$ cm^{-3} (temperature range 96–113 K). The shortest time range for peak B3 is 65 kyr, corresponding to a temperature range of 102–132 K at $n = 10^9$ cm^{-3}. These time ranges are not reasonable, as the gas in the disk would have made several revolutions during such a long period.

The fiducial model fits peaks B1/B2 and core A very well using a fast warm-up. Abundances toward peaks B1/B2 can even be reproduced within a time period of 1.3 kyr at a gas density of 10^8 cm^{-3}. Core A requires a longer time period of 6.4 kyr, but is still well fit at a gas density of 10^8 cm^{-3} with a fast warm-up. The best fit models for B1/B2 and A are shown in Fig. 6. The abundances of C_2H_5CN toward peak B3 cannot be reproduced using a fast warm-up, but the shortest time period (13 kyr) that reproduces all abundances is using a medium warm-up at a gas density of 10^7 cm^{-3}. This is too long kinematically (the disk rotational period is ~10 kyr), and we expect it to be a high-mass source with a fast warm-up time because it has a high luminosity, cluster of OH masers (Hutawarakorn & Cohen 1999), and a high kinetic temperature (~300 K) together with a high deuterium fraction implying that it has recently heated up very quickly (Allen et al. 2017). As our model does not use any reactions with deuterium, we can only assume that the model abundances may differ from those listed if these reactions were included.

For nearly all warm-up speeds and densities, the lower time range is constrained by the HC_3N abundance in core A and source B3 and by CH_3CN in B1/B2. Where this is not the case, CH_3OCHO is the lower abundance constraint. The upper time range is constrained by the C_2H_5CN abundance for source B3 and core A in medium and slow warm-ups and by CH_2CHCN in fast warm-ups, where source B3 cannot be reproduced because of the high C_2H_5CN abundance. The C_2H_5OH abundance provides the upper time range constraint for sources B1/B2 in most cases, but the CH_3OCHO abundance provides the upper limit for the fast warm-up at 10^7 cm^{-3} and the slow warm-up at 10^8 cm^{-3} and CH_3CHO is the upper constraining species for the medium and slow warm-ups at 10^9 cm^{-3}.

When investigating the time ranges for B1/B2 observations for the abundances of the unobserved cyanides (CH_2CHCN and C_2H_5CN), we see that they are very low (between 10^{-10} and 10^{-14} for all models). The abundances of these species increase rapidly in a short space of time. The most dramatic is C_2H_5CN

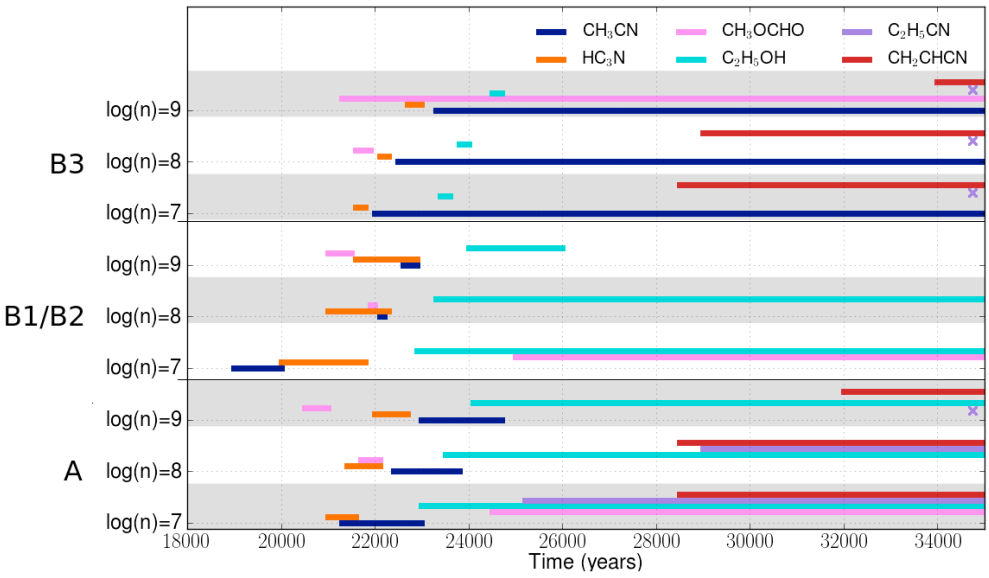

Fig. 5. Time periods for which the observed abundances of HC_3N, CH_3CN, CH_2CHCN, C_2H_5CN, CH_3OCHO, and CH_2H_5OH are reproduced. The purple "X" marks indicate that the abundance of C_2H_5CN is not reproduced for this source and gas density.

which jumps up 2 orders of magnitude within 1000 years in the fast warm-up at $n = 10^7$ cm^{-3} (a temperature change of ∼10 K).

3.2. Reaction–diffusion competition excluded

Reaction–diffusion competition is a mechanism used in chemical modeling to allow grain-surface reactions with energy barriers to proceed more easily. This mechanism compares the relative timescales between the reaction of two species and their diffusion to determine which process will occur (Cuppen et al. 2017). Because reaction–diffusion competition may be overexpressed in a two-phase chemical model (gas and ice), we modeled a test case without it. In this case, key species such as CH_3OH, CH_3OCHO, and C_2H_5OH are underproduced by as much as 2 orders of magnitude compared to the lower limit abundances for any of our observed sources. Figure 7 demonstrates one instance where all three of these species are underproduced for B1-2. More efficient grain-surface chemistry facilitated by reaction–diffusion competition is required to better match the observations, which should be tested in more detailed three-phase chemical models.

3.3. Varying the initial temperature

It is plausible that for high-mass stars forming in a cluster, possibly sequentially, an initial temperature of 10 K is an underestimation (Tieftrunk et al. 1998). For this reason we also modeled the chemistry of dense gas warming up from 15 to 25 K. Looking at the changes in abundance for constraining species, CH_3OCHO, HC_3N, and C_2H_5CN, we see that increasing starting temperatures decrease the abundances of CH_3OCHO and C_2H_5CN but increase the abundance of HC_3N (see Fig. 8). For C_2H_5CN, longer times at as a low temperature allows more to form in the ice, to be later released into the gas phase.

Because the warm-up is exponential, starting at 15 K rather than 10 K results in 6000 years less at a low temperature (and 10 000 for 25 K) for the fast warm-up. Since the formation path to C_2H_5CN is mainly in the ice it appears that time at a low temperature is critical. This is demonstrated as well in the medium and slow warm-ups in which high abundances of C_2H_5CN are made as these models spend a very long time at low temperatures. The temperature range between 15 and 30 K is critical for grain-surface reactions because the dust temperature determines the sticking efficiency of volatile species (such as H, H_2, and CO). At higher temperatures hydrogenation pathways (such as those that lead to C_2H_5CN) are less likely to occur.

3.4. Continuing with constant high temperature gas-phase chemistry

To investigate the effect of high temperature gas-phase chemistry on our final abundances in the fast warm-up, we modeled warming up the dense gas to 300 K, then continued at that temperature for an additional 40 kyr. As C_2H_5CN is the only species that cannot be fit for source B3, we focus on the abundance of this species produced at different densities with extra time to perform gas-phase chemistry. In Fig. 9, we see that the abundances produced after 300 K do not deviate from those when the gas continues to warm to 500 K. In the extra time, abundances only increase at the highest gas density and then by 36% ($\sim 1 \times 10^{-11}$), which does not reproduce the observed minimum abundance.

3.5. HCN as an initial ice species

HCN has been observed in cometary ice (Mumma & Charnley 2011; Le Roy et al. 2015) and is expected to occur in ices around protostars but has not yet been detected (Boogert et al. 2015). To test the effect of including HCN in the ice, we modeled the following three additional initial abundances of HCN ice: 0.1%, 1%, and 10% vs. H_2O. An abundance of 0.1% reflects the observed abundance in cometary ice (0.08–0.5%), but the higher abundances were used to test if there was any increase in our CN-bearing species using an unrealistic concentration of HCN. In Fig. 10 we see that the constraining species are barely affected by this change in HCN abundance, while the HCN gas abundances are directly affected. We conclude that HCN is not an important progenitor to any of the nitrogen-bearing species that we are focusing on and for the range of physical conditions explored in this work.

3.6. Varying the cosmic-ray ionization rate

The fiducial model uses a low cosmic-ray ionization rate commonly used in chemical modeling of 1.3×10^{-17} s^{-1}, which is low compared with more distant observed star-forming regions (Indriolo et al. 2015). We modeled the chemistry over time

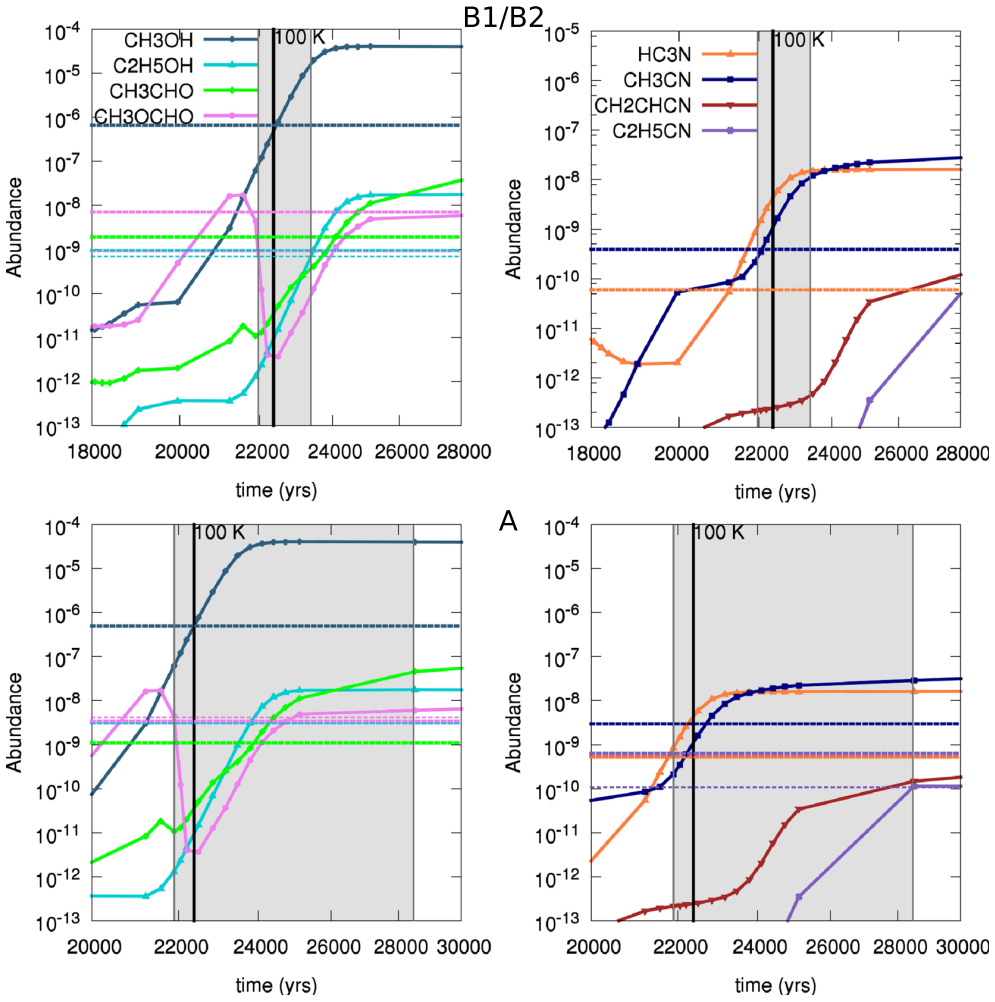

Fig. 6. Best fit models of abundances vs. H_2 for CH_3OH, C_2H_5OH, CH_3CHO, CH_3OCHO, HC_3N, CH_3CN, CH_2CHCN, and C_2H_5CN using IC 5. G35.20 B1/B2 (*top*) is best fit by the fast model with a gas density of 10^8 cm^{-3} over a time period of 1.3 kyr. G35.20 A (*bottom*) is also best fit by the fast model with a gas density of 10^8 cm^{-3} over a time period of 6.4 kyr. The line colors for A are the same as B1/B2 as shown in the key. All species are shown in the key with color-coded dashed horizontal lines showing the observed abundances for the source. The thinner dashed lines indicate the upper limit and lower limit species that best constrain the time span. The time ranges in which all abundances can be reproduced within the errors reported in Appendix B are shaded. We truncate the *x*-axis scale to better highlight the chemistry changes over the temperature range at which the COMs are released from the ice mantles.

Table 4. Time ranges (in kyr) that are needed fit observed abundances in the lower abundance sources, B1/B2, those for the higher abundance source, B3, at a cosmic-ray ionization rate of 1×10^{-16} s^{-1} in a fast warm up.

Density	B1/B2		B3	
(cm^{-3})	Time range (kyr)	T_{gas} (K)	Time range (kyr)	T_{gas} (K)
10^7	19–22.75	74–101	21.25–25	90–123
10^8	20–23	81–105	21.9–25.4	96–127
10^9	22.3–23.6	99–110	22.7–26	108–132

Notes. Corresponding temperatures are also shown (in K).

for two higher cosmic-ray ionization rates, 1×10^{-16} s^{-1} and 6×10^{-16} s^{-1}, to be comparable to the mean and uppermost values from Indriolo et al. (2015). When comparing the changes in abundance for constraining species, CH_3CN, CH_3OCHO, HC_3N, and C_2H_5CN, we see that a higher cosmic-ray ionization rate increases their abundances, although after ~25 kyr the abundances for a cosmic-ray ionization rate of 6×10^{-16} s^{-1} drop sharply (see Fig. 11). This sharp drop in our key species is due to either a high abundance of H_3O^+ and $HNCH^+$ in the case of CH_3CN, CH_3OCHO, and HC_3N, or dissociation by cosmic rays for C_2H_5CN. A cosmic-ray ionization rate of 1×10^{-16} s^{-1} presents a solution that fits the observed abundances in source B3 with a fast warm-up.

The shortest time period that fits the observed abundances in source B3 is 3.3 kyr in a fast warm-up with a cosmic-ray ionization rate of 1×10^{-16} s^{-1} and a gas density of 10^9 cm^{-3} (Fig. 12). The observed abundances of A and B1-2 are also well fit with a cosmic-ray ionization rate of 1×10^{-16} s^{-1}. A rate of 6×10^{-16} s^{-1} raises the modeled abundance of HC_3N such that it no longer fits any of the observed abundances and so is not a viable solution for the model assumptions and parameters explored here. Table A.1 summarizes the time ranges where the model abundances fit the observed abundances at a cosmic-ray ionization rate of 1×10^{-16} s^{-1}, with corresponding temperatures. It is clear that for the same H_2 density and cosmic-ray ionization rate, there is a small time overlap between sources B1/B2 and source B3, and B3 is always a few thousand years older than B1/B2.

3.7. Dominant formation routes

We studied the reactions behind each of our eight focus species to determine whether they were formed mostly through ice processing and sublimation, through gas-phase formation following the sublimation of their precursors, or a mixture of both.

CH_3OH, HC_3N, and C_2H_5CN are predominantly produced on the grain surfaces then sublimated with little to no gas-phase production. Significant amounts of CH_3CN are produced on the grain surface, but after sublimation gas-phase processes increase the abundance of CH_3CN gas to ~8 times the maximum ice abundance. C_2H_5OH is also produced predominantly in the ice, but gas processes double the maximum ice abundance.

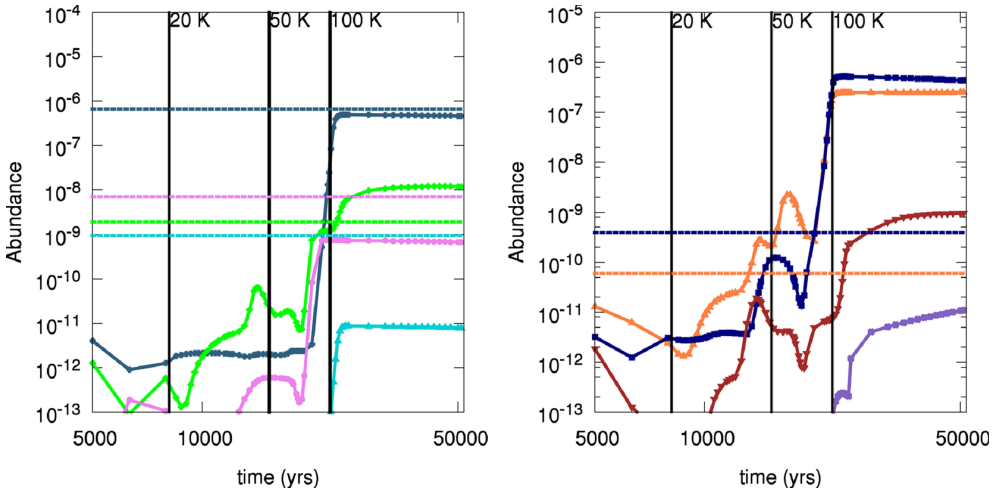

Fig. 7. Fractional abundance for B1-2 fast warm-up (from 10 to 500 K) model at a gas density of 10^7 cm^{-3} for the time period 5–50 kyr without reaction–diffusion competition. All species are color coded as in Fig. 6 with horizontal lines showing the observed abundances for B1/B2. The abundances of CH_3OH, CH_3OCHO, and C_2H_5OH are not reproduced.

The ice and gas-phase abundances of CH_3CHO are unusual in that the ice abundance drops sharply around 63–70 K in the fast warm-up (at different densities). This appears to coincide with an increase in CH_3OH and CH_3OCHO gas abundances. At this temperature in the model, grain surface CH_3CHO reacts with CH_2OH to form either C_2H_5OH and HCO or CH_3 and CH_2OHCHO in the ice, or it reacts with NH_2 to form NH_3 and CH_3CO in the ice as well. CH_2OHCHO is important in forming CH_3OH and CH_3OCHO on grain surfaces. The CH_3CHO gas abundance does not increase until the temperature reaches ~100 K. At that temperature, the main production pathway is through neutral-neutral reactions between CH_3OH and CH in the gas phase. So despite the significant abundances of CH_3CHO that are produced in the ice, very little of this sublimates into the gas phase. The CH_3CHO gas is mainly a product of CH_3OH and CH.

CH_3OCHO is made abundantly in the ice, but reacts with OH in the ice to form $COOCH_3$ and water ice by hydrogen abstraction. $COOCH_3$ is hydrogenated in the ice and the resulting CH_3OCHO is released to the gas ($H_{(ice)} + COOCH_{3(ice)} = CH_3OCHO$). This is the main mechanism for creating CH_3OCHO in the gas rather than sublimation of CH_3OCHO from the ice or formation in the gas.

CH_2CHCN is another species that can be made at low fractional abundances (10^{-12}–10^{-10}) in the ice and gas. Ice phase CH_2CHCN is dominantly produced through the dissociation of C_2H_5CN by cosmic rays, whereas the gas-phase formation route is the reaction of CN with either C_2H_4 or CH_3CHCH_2. After a temperature of ~115 K, the CH_2CHCN in the ice is sublimated and adds to the gas-phase abundance.

4. Discussion

4.1. General test differences

The first interesting result is that our model abundances are almost independent of initial ice conditions that we used, which are constrained by the observations of Gibb et al. (2004) and theoretical abundance ratios from van Dishoeck (2004). The range of ice abundances in our different IC sets is not large, but it is based on real sources. The models suggest that the initial ice composition is not crucial to modeling the chemical composition of a later state, thereby showing that the warm-up stage determines the composition of the hot core. It is possible that adding molecular gas to the initial conditions would have an effect on the final abundances; however, such a parameter-space exploration of the initial gas composition requires a dedicated suite of models and is beyond the scope of this work. This should be carried out in the future.

The second interesting result is a much debated topic in chemical modeling (Cuppen et al. 2017): the importance of approximating reaction–diffusion competition in rate equation based models. In this work, in order to reproduce the lower limit abundances of the species that we focus on from G35.20, reaction–diffusion competition is needed, otherwise oxygen-bearing complex organic species are underproduced by as much as 2 orders of magnitude. Reaction–diffusion competition has also been shown to be necessary in the work of Ruaud et al. (2016) and Quénard et al. (2018) among others, but it is important to note that gas-phase reactions for COMs in chemical networks have also been shown to be incomplete (Balucani et al. 2015).

The modeled gas temperatures at which the abundances are reproduced are lower than the kinetic temperatures (300 K for source B3, 285 K for core A, 160 K for source B1, 120 K for source B2) determined in Allen et al. (2017). The gas temperatures from our chemical model are 110-130 K for source B3, 100-110 K for sources B1/B2, and 100-130 K for core A. As we have demonstrated that increasing the temperature and running the chemistry for longer does not significantly affect the final abundances, then the reproduction of the observed abundances at lower temperatures is an advantage.

4.2. Reproducing source B3

In our fiducial model, the warm-up time is the most significant factor in reproducing the abundances of the observed species. The high abundances of C_2H_5CN seen in source B3 cannot be produced in a fast warm-up in our fiducial model. While relatively short time ranges can be found to reproduce the abundances seen in sources B1/B2 in any of our models (with the shortest time range of 1.3 kyr from a fast model at 10^8 cm^{-3}), those of source B3 can only be reproduced in medium or slow warm-up models. These longer warm-up times imply a lower mass protostar. Observational evidence points to source B3 being associated with a high-mass protostar: there are numerous masers about its position and the kinetic temperature is high (~300 K). On the other hand, a high deuterium fraction (13%) for CH_3CN (Allen et al. 2017) indicates that it was recently very cold and therefore needs a faster warm-up time.

We reproduced the observed abundances in source B3 well using a cosmic-ray ionization rate a few times higher than in the standard value (van der Tak & van Dishoeck 2000) for

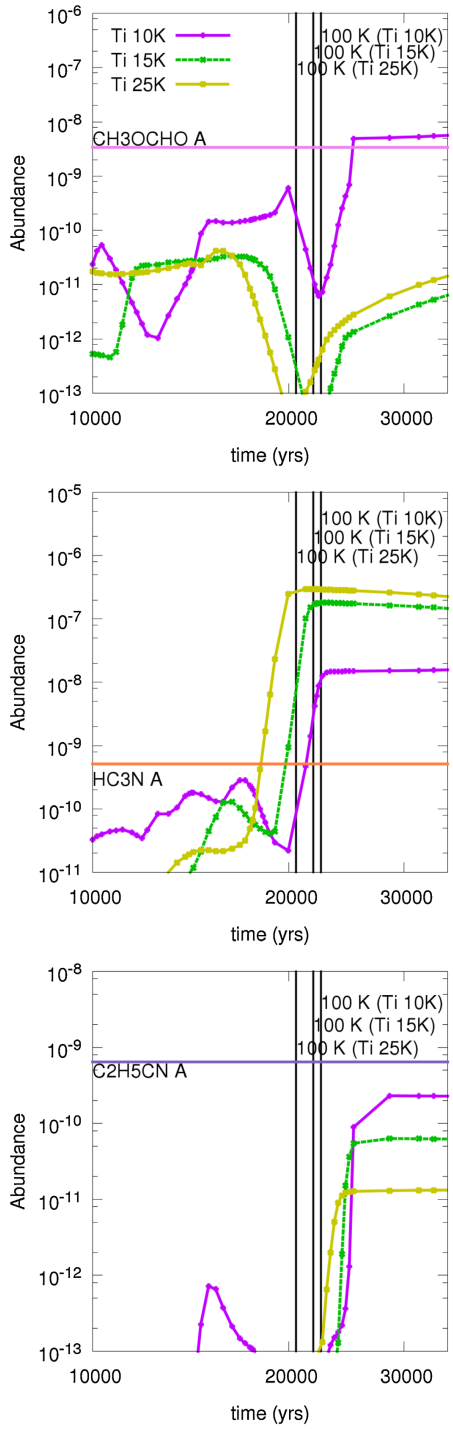

Fig. 8. Comparing the fractional abundances for three constraining species, CH_3OCHO (*top*), HC_3N (*middle*), and C_2H_5CN (*bottom*), using different initial temperatures (10 K in magenta, 15 K in green, and 25 K in yellow) at a gas density of 10^7 cm^{-3} for a fast warm-up. The vertical lines show the time corresponding to a temperature of 100 K for each initial temperature. The observed abundances (horizontal lines) for G35.20 A are shown for reference.

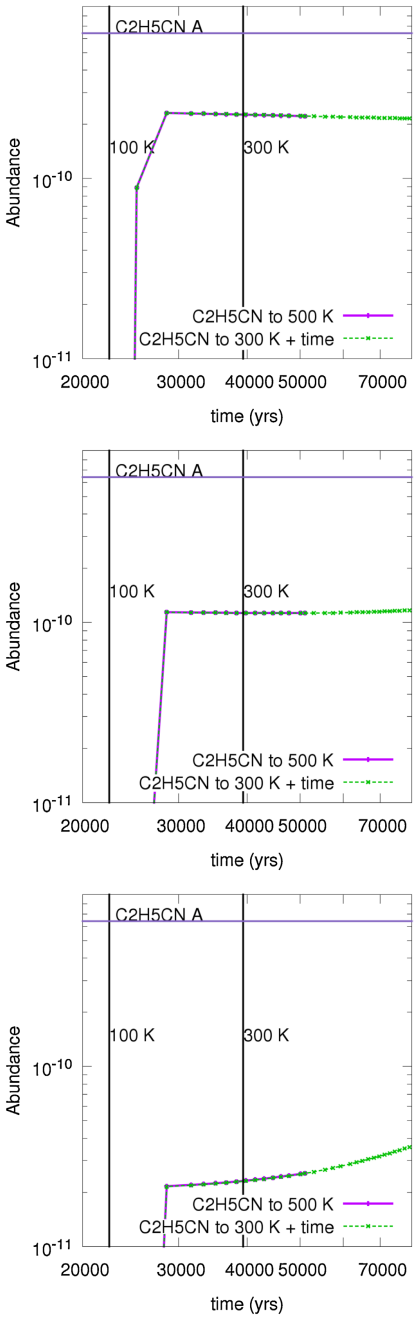

Fig. 9. Fractional abundances for C_2H_5CN comparing warming up to 500 K with warming up to 300 K then continuing at a constant temperature at densities of 10^7 cm^{-3} (*top*), 10^8 cm^{-3} (*middle*), and 10^9 cm^{-3} (*bottom*) for a fast warm-up. The observed abundance (horizontal lines) for G35.20 A is shown for reference.

the interstellar medium. A higher mean cosmic-ray ionization rate of 1.78×10^{-16} s^{-1} was found in observations by Indriolo et al. (2015) and our models seem to agree with this higher rate. Source B1/B2 is also well reproduced within a 1.3 kyr time period using a cosmic-ray ionization rate of 1×10^{-16} s^{-1}, without the abundances of the complex cyanides becoming too high.

It is possible that adding gas-phase reactions forming C_2H_5CN to the network will make it possible to reproduce the higher abundances seen in source B3 with the fiducial model, as the network currently contains no gas-phase reactions to produce this species. Such reactions are not often tested in the laboratory as cyanides are dangerous to work with, but it would be extremely useful for labs to test these reactions in the future to improve the chemical networks.

4.3. Warm-up times

The Garrod models (Garrod & Herbst 2006; Garrod et al. 2008) and their predecessor models (Viti & Williams 1999) derive their

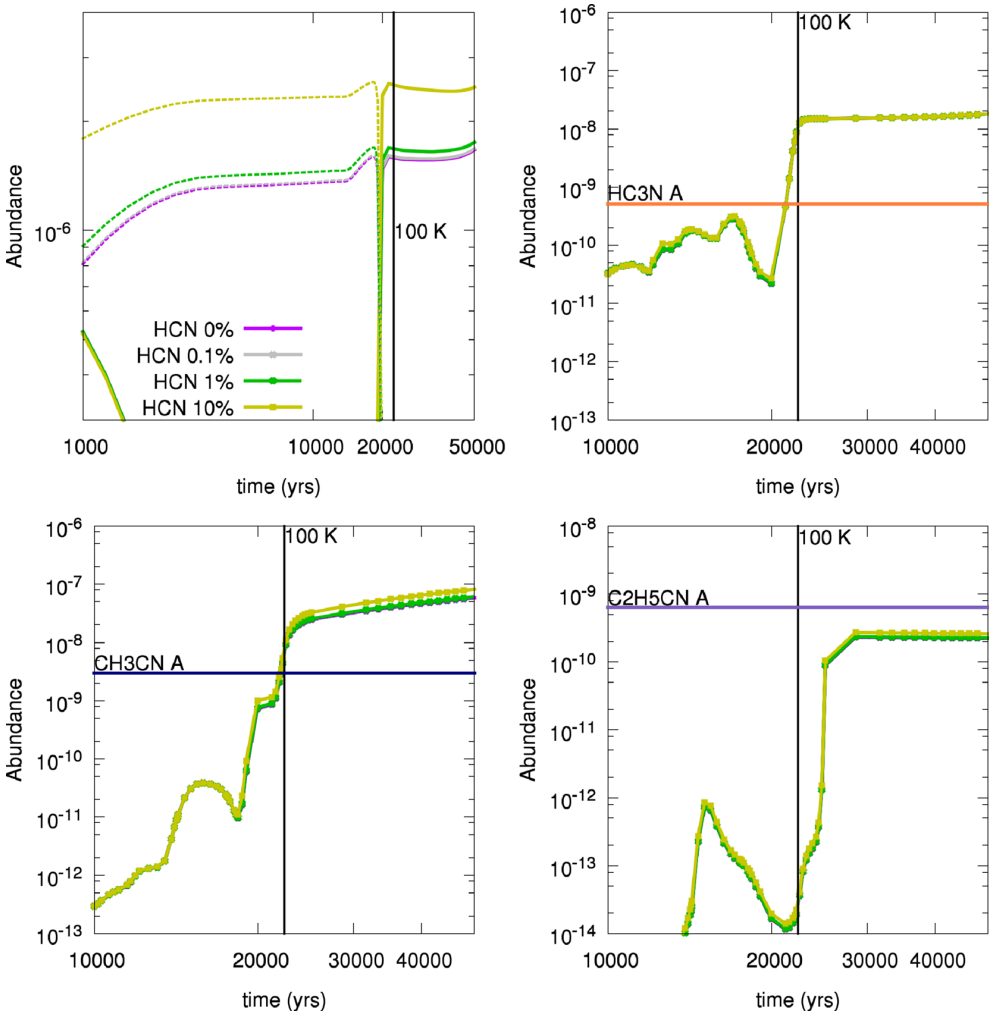

Fig. 10. Fractional abundances for nitrogen-bearing species with a gas density of 10^7 cm^{-3} and a fast warm-up. HCN gas (solid lines) and ice (dashed lines) abundances with the color key for all four panels (*top left*), HC_3N gas (*top right*), CH_3CN gas (*bottom left*), and C_2H_5CN gas (*bottom right*) abundances over time are shown for four initial HCN ice abundances (0, 0.1, 1, and 10%). The observed abundances (horizontal lines) for G35.20 A are shown for reference.

warm-up times from the work of Bernasconi & Maeder (1996; BM96 from here on). In BM96 work, the contraction times for different masses of stars (from 0.8 to 60 $M_\odot$) are determined under the assumption that the accretion rate is between 10^{-5} and 10^{-4} $M_\odot$ yr^{-1}. It has been reported more recently that mass accretion rates can be as high as 10^{-3} $M_\odot$ yr^{-1} (Tan et al. 2014), although this may be episodic. Hosokawa & Omukai (2009) found that these high accretion rates led to pre-main sequence stars with larger-than-typical radii. Ramírez-Tannus et al. (2017) has recently reported observational evidence for this in M17. In any case, our fast, medium, and slow warm-up times correspond to 60, 15, and 6 $M_\odot$ objects from the original BM96 paper, considered to be very high, high, and intermediate mass sources. If we assume that the accretion rate of our objects is ten times higher and decrease the contraction times of the BM96 objects accordingly, that gives more reasonable stellar masses of 8, 4, and 1 $M_\odot$ for the fast, medium, and slow warm ups, respectively. This is not a strictly accurate way of determining the relationship between mass at warm-up time, but it leads to much more reasonable masses and takes into account the observational and theoretical work that has been carried out since BM96 was published.

5. Conclusions

The disagreement between the disk-like kinematics of the high-mass star-forming region in G35.20−0.74 B and its chemical segregation across its individual cores is not easily explained. The high cyanide abundances observed toward peak B3 can be reproduced in a fast warm-up, but only with a higher cosmic-ray ionization rate of 1×10^{-16} s^{-1}. The smallest time period required to reproduce the abundances in source B3 is 3.3 kyr at a gas density of 10^9 cm^{-3}. This is a reasonable cosmic-ray ionization rate as evidenced by observations by Indriolo et al. (2015). The abundances observed in the rest of the disk candidate (B1/B2) can easily be reproduced with a fast warm-up at a gas density of 10^8 cm^{-3} and a low rate of cosmic-ray ionization in a very short time period (∼1.3 kyr), but can also be reproduced with the higher cosmic-ray ionization rate of 1×10^{-16} s^{-1} at a gas density of 10^9 cm^{-3} in 1.3 kyr.

We find that the abundance of ethyl cyanide in particular is maximized in models with a low initial temperature, a high cosmic-ray ionization rate, a long warm-up time, or a lower gas density. The model is most sensitive to age in the context of a warm-up model (therefore temperature), and to cosmic-ray ionization rate. It is not sensitive to the initial ice composition (within observed ranges) and not strongly dependent on gas density showing that the warm-up phase determines the composition.

If we assume that the cosmic-ray ionization rate is the same around sources B1/B2 and source B3 at 1×10^{-16} s^{-1} and the sources have a gas density of 10^9 cm^{-3}, then the age of sources B1/B2 is 22.3–23.6 kyr while the age of source B3 is 22.7–26 kyr. This indicates that both these sources began forming within a few thousand years and source B3 is 2000 years older. Based on an outer disk rotation period between 9700 and

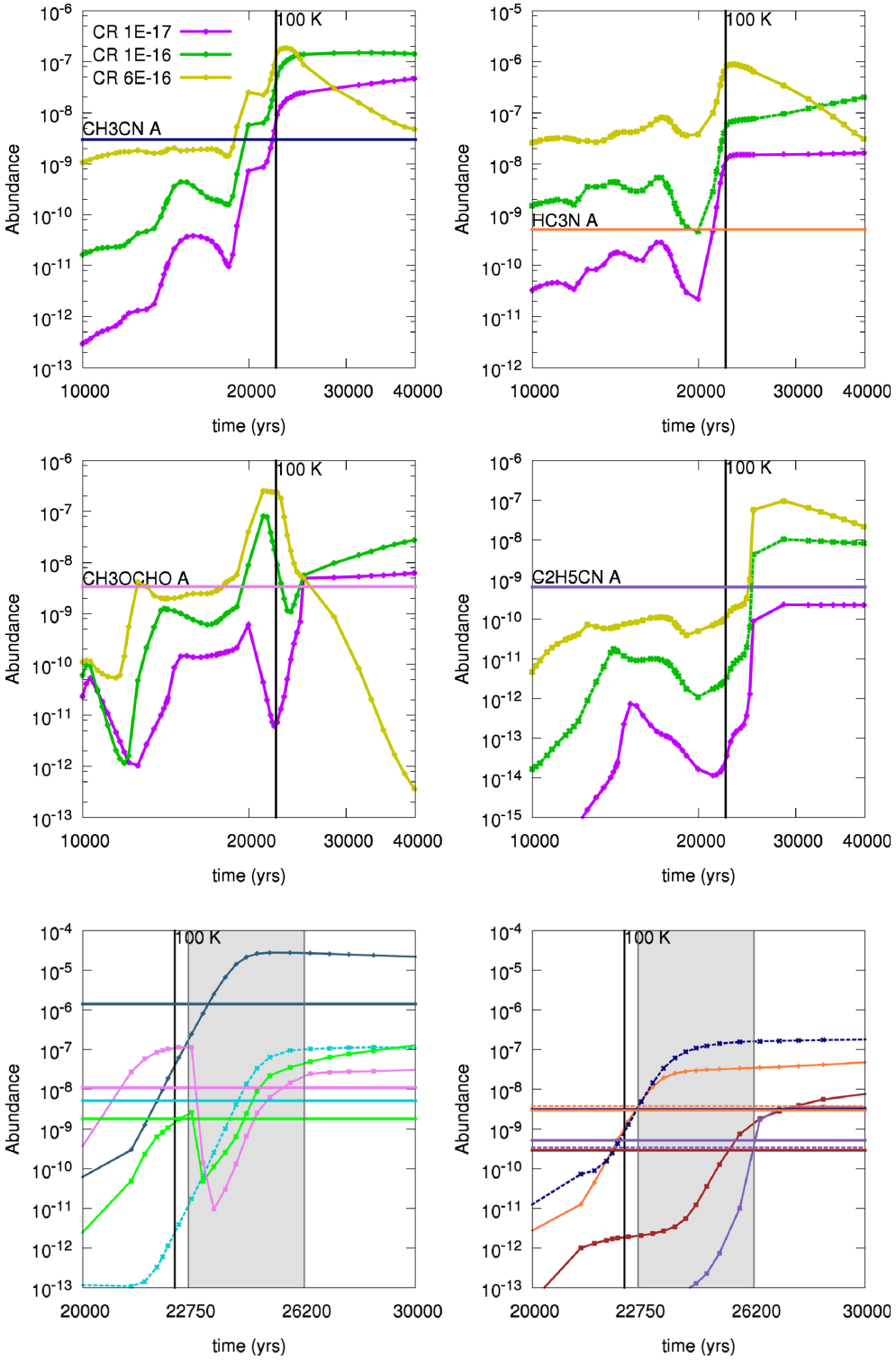

Fig. 11. Comparing fractional abundances for four constraining species with different cosmic-ray ionization rates with a gas density of 10^7 cm^{-3} for a fast warm-up. CH_3CN with the color key for all four panels (*top left*), HC_3N (*top right*), CH_3OCHO (*bottom left*), and C_2H_5CN gas (*bottom right*) abundances over time are shown for three cosmic-ray ionization rates (1.3×10^{-17}, 1×10^{-16}, and 6×10^{-16} s^{-1}). The observed abundances (horizontal lines) for G35.20 A are shown for reference.

Fig. 12. Fractional abundances for source B3 with a cosmic-ray ionization rate of 1×10^{-16} s^{-1}, a gas density of 10^9 cm^{-3} for a fast warm-up. All species are shown in the key with color-coded dashed horizontal lines showing the observed abundances for source B3. The thinner dashed lines indicate the upper limit for HC_3N and the lower limit for C_2H_5CN, as they are the species that constrain the time span. The best fit time period of 3.4 kyr is shaded. The colors are coded as in Fig. 6.

11 100 years, this age difference is physically possible. So we conclude that the detection of CH_2CHCN and C_2H_5CN can indicate a lower limit for the age of a hot core and a nondetection indicates an upper age limit. This can be useful when observing a potential multiple system at a lower resolution, where if CH_2CHCN or C_2H_5CN is detected toward one part of a source and undetected in others, it indicates a young high-mass system with protostars of different ages.

We have covered a variety of star formation scenarios including a range of gas densities, regions with triggered star formation (starting at temperatures above 10 K), regions with higher and lower cosmic-ray ionization rates, and a range of masses (via warm-up speeds). With this coverage of parameter space we propose that these model results can be used to interpret and predict observations from a variety of embedded high-mass sources and intend to investigate other sources in the future. While we have explored the parameter space in these models comprehensively and noted the trends arising from this analysis, there is still much work to be carried out theoretically and experimentally to understand the gas and ice chemistry of cyanides. Without this work, our ability to study complex cyanide chemistry will remain hindered.

Acknowledgements. We would like to thank our referee, Professor Serena Viti, for her constructive comments and quick reading. The PhD project of V. Allen is funded by the Netherlands Organisation for Scientific Research (NWO) and Netherlands Institute for Space Research (SRON). C. Walsh acknowledges NWO (program 639.041.335) and the University of Leeds for financial support.

References

Allen, V., van der Tak, F. F. S., Sánchez-Monge, Á., Cesaroni, R., & Beltrán, M. T. 2017, A&A, 603, A133
Balucani, N., Ceccarelli, C., & Taquet, V. 2015, MNRAS, 449, L16
Bernasconi, P. A., & Maeder, A. 1996, A&A, 307, 829
Blake, G. A., Sutton, E. C., Masson, C. R., & Phillips, T. G. 1987, ApJ, 315, 621
Boogert, A. C. A., Gerakines, P. A., & Whittet, D. C. B. 2015, ARA&A, 53, 541
Caselli, P., Hasegawa, T. I., & Herbst, E. 1993, ApJ, 408, 548
Crockett, N. R., Bergin, E. A., Neill, J. L., et al. 2015, ApJ, 806, 239
Cuppen, H. M., Walsh, C., Lamberts, T., et al. 2017, Space Sci. Rev., 212, 1
Drozdovskaya, M. N., Walsh, C., Visser, R., Harsono, D., & van Dishoeck E. F. 2014, MNRAS, 445, 913
Feng, S., Beuther, H., Henning, T., et al. 2015, A&A, 581, A71
Garrod, R. T., & Herbst, E. 2006, A&A, 457, 927
Garrod, R. T., Widicus Weaver, S. L., & Herbst, E. 2008, ApJ, 682, 283
Gibb, E. L., Whittet, D. C. B., Boogert, A. C. A., & Tielens, A. G. G. M. 2004, ApJS, 151, 35
Herbst, E., & van Dishoeck E. F. 2009, ARA&A, 47, 427
Hosokawa, T., & Omukai, K. 2009, ApJ, 691, 823
Hutawarakorn, B., & Cohen, R. J. 1999, MNRAS, 303, 845
Indriolo, N., Neufeld, D. A., Gerin, M., et al. 2015, ApJ, 800, 40
Jiménez-Serra, I., Zhang, Q., Viti, S., Martín-Pintado, J., & de Wit W.-J. 2012, ApJ, 753, 34
Koumpia, E., van der Tak, F. F. S., Kwon, W., et al. 2016, A&A, 595, A51
Le Roy, L., Altwegg, K., Balsiger, H., et al. 2015, A&A, 583, A1
McElroy, D., Walsh, C., Markwick, A. J., et al. 2013, A&A, 550, A36
Möller, T., Endres, C., & Schilke, P. 2017, A&A, 598, A7
Mumma, M. J., & Charnley, S. B. 2011, ARA&A, 49, 471
Penteado, E. M., Walsh, C., & Cuppen, H. M. 2017, ApJ, 844, 71
Quénard, D., Jiménez-Serra, I., Viti, S., Holdship, J., & Coutens, A. 2018, MNRAS, 474, 2796
Ramírez-Tannus, M. C., Kaper, L., de Koter, A., et al. 2017, A&A, 604, A78
Ruaud, M., Wakelam, V., & Hersant, F. 2016, MNRAS, 459, 3756
Ruoskanen, J., Harju, J., Juvela, M., et al. 2011, A&A, 534, A122
Sánchez-Monge, Á., Cesaroni, R., Beltrán, M. T., et al. 2013, A&A, 552, L10
Sánchez-Monge, Á., Beltrán, M. T., Cesaroni, R., et al. 2014, A&A, 569, A11
Tan, J. C., Beltrán, M. T., Caselli, P., et al. 2014, Protostars and Planets VI, eds. H. Beuther, R. S. Klessen, C. P. Dullemond, & T. Henning (Tucson: University of Arizona Press), 149
Tieftrunk, A. R., Gaume, R. A., & Wilson, T. L. 1998, A&A, 340, 232
van der Tak, F. F. S., & van Dishoeck E. F. 2000, A&A, 358, L79
van Dishoeck, E. F. 2004, ARA&A, 42, 119
Vastel, C., Ceccarelli, C., Lefloch, B., & Bachiller, R. 2016, A&A, 591, L2
Viti, S., & Williams, D. A. 1999, MNRAS, 305, 755
Viti, S., Collings, M. P., Dever, J. W., McCoustra, M. R. S., & Williams, D. A. 2004, MNRAS, 354, 1141
Walsh, C., Millar, T. J., Nomura, H., et al. 2014, A&A, 563, A33
Walsh, C., Nomura, H., & van Dishoeck E. 2015, A&A, 582, A88
Wyrowski, F., Schilke, P., Walmsley, C. M., & Menten, K. M. 1999, ApJ, 514, L43

Appendix A: Initial conditions

Table A.1. Full initial conditions (abundance of each species vs. total composition).

Species	Initial conditions 1	Initial conditions 2	Initial conditions 3	Initial conditions 4	Initial conditions 5
H (gas)	3.525×10^{-5}	2.560×10^{-5}	0	1.880×10^{-5}	2.270×10^{-5}
C (gas)	1.375×10^{-4}	1.367×10^{-4}	1.150×10^{-4}	1.357×10^{-4}	1.3875×10^{-4}
N (gas)	7.475×10^{-5}	7.480×10^{-5}	7.250×10^{-5}	7.350×10^{-5}	7.350×10^{-5}
O (gas)	3.118×10^{-4}	3.048×10^{-4}	2.375×10^{-4}	3.0385×10^{-4}	3.029×10^{-4}
H_2O (ice)	5.0×10^{-6}	1.0×10^{-5}	5.0×10^{-5}	1.0×10^{-5}	1.0×10^{-5}
CO (ice)	5.0×10^{-7}	5.0×10^{-7}	5.0×10^{-6}	8.0×10^{-7}	1.7×10^{-6}
CO_2 (ice)	5.0×10^{-7}	1.5×10^{-6}	5.0×10^{-6}	1.3×10^{-6}	2.3×10^{-6}
NH_3 (ice)	2.5×10^{-7}	2.0×10^{-7}	2.5×10^{-6}	1.5×10^{-6}	1.5×10^{-6}
CH_3OH (ice)	2.5×10^{-7}	5.0×10^{-7}	2.5×10^{-6}	1.0×10^{-6}	4.0×10^{-7}
HCOOH (ice)	5.0×10^{-7}	5.0×10^{-7}	5.0×10^{-6}	7.0×10^{-7}	1.0×10^{-7}
CH_4 (ice)	2.5×10^{-7}	1.0×10^{-7}	2.5×10^{-6}	1.5×10^{-7}	1.5×10^{-7}
H_2CO (ice)	5.0×10^{-7}	2.0×10^{-7}	5.0×10^{-6}	3.5×10^{-7}	2.0×10^{-7}

Notes. It is assumed that all available atomic hydrogen is in the form of H_2. IC1 is based on a lower limit of the water abundance of 10^{-5} vs. H_2 and IC 3 is based on the upper limit of water abundance of 10^{-4} vs. H_2. For IC 2, 4, and 5 the water ice abundance is set at 5×10^{-5} vs. H_2 and the other ice abundances are calculated from percentages vs. water from observations of ice in star-forming regions (Gibb et al. 2004). IC2 is based on AFGL 2136, IC4 on W33A, and IC5 on NGC7538 IRS9.

Appendix B: Abundance ranges with errors

Table B.1. Abundance range observed in Allen et al. (2017).

Species	A			B1/B2			B3		
	Abundance	Lower	Upper	Abundance	Lower	Upper	Abundance	Lower	Upper
CH_3OH	5.04×10^{-7}	1.02×10^{-7}	1.96×10^{-6}	6.68×10^{-7}	2.05×10^{-7}	4.55×10^{-5}	1.36×10^{-6}	1.05×10^{-6}	1.71×10^{-6}
C_2H_5OH	2.97×10^{-9}	9.28×10^{-10}	3.33×10^{-8}	9.42×10^{-10}	6.85×10^{-10}	1.56×10^{-8}	5.15×10^{-9}	4.08×10^{-9}	6.02×10^{-9}
CH_3CHO	1.11×10^{-9}	3.44×10^{-11}	4.17×10^{-9}	1.88×10^{-9}	1.78×10^{-10}	7.11×10^{-9}	1.76×10^{-9}	1.12×10^{-9}	7.56×10^{-9}
CH_3OCHO	3.38×10^{-9}	4.30×10^{-10}	4.17×10^{-9}	7.02×10^{-9}	8.80×10^{-10}	1.56×10^{-8}	1.10×10^{-8}	9.45×10^{-9}	1.72×10^{-8}
CH_3CN	2.97×10^{-9}	9.39×10^{-10}	1.50×10^{-8}	3.93×10^{-10}	3.65×10^{-10}	5.29×10^{-10}	3.10×10^{-9}	2.31×10^{-9}	4.04×10^{-7}
CH_2CHCN	5.33×10^{-10}	1.44×10^{-10}	1.46×10^{-9}	Upper limit 2×10^{-13}			2.92×10^{-10}	1.63×10^{-10}	4.00×10^{-9}
C_2H_5CN	6.37×10^{-10}	1.07×10^{-10}	1.25×10^{-9}	Upper limit 1×10^{-13}			5.15×10^{-10}	3.40×10^{-10}	7.98×10^{-10}
HC_3N	5.13×10^{-10}	1.42×10^{-10}	1.83×10^{-9}	5.93×10^{-11}	4.79×10^{-11}	3.03×10^{-9}	3.05×10^{-9}	2.40×10^{-9}	3.75×10^{-9}

Notes. Columns 2, 5, and 8 are the best fit abundances; 3, 6, and 9 are the lower limit to the abundances from error calculations; and 4, 7, and 10 are the upper limits to abundances. CH_2CHCN and C_2H_5CN were not detected in B1 or B2 so their abundances are an upper limit.

Appendix C: Comparison with Garrod et al. (2008)

We compared our model without reaction–diffusion competition to the well-known model in Garrod et al. (2008) and found significant differences. At all warm-up speeds the difference between our abundances and their reduced model is 1 to 4 orders of magnitude for more complex species, while the abundances of simpler species (H_2O, CO, NH_3, and CH_4) are similar to those in Garrod et al. (2008). The model abundances from Garrod et al. (2008) cannot reproduce the observed abundances in G35.20 B3, as the fractional abundances of C_2H_5OH, CH_3OCHO, and CH_3CHO are at least one order of magnitude too low. These authors did not report abundances of CH_2CHCN or C_2H_5CN so that cannot be compared. There are some notable differences between our model results and those of Garrod. The initial ice composition not the same, although we found that the initial ice composition does not strongly affect the final abundances. Without knowing their grain-surface parameters, that cannot be compared. Garrod et al. also used a different gas network from us (UMIST vs. OSU) and both networks have been updated significantly since 2008. Most updates to the networks involve updating the binding energies of surface species (Penteado et al. 2017). We also take further steps in varying the cosmic-ray ionization rate and gas densities to investigate the effect of these parameters on the chemical make-up of our modeled sources.

Appendix D: Time ranges

Tables and figures showing the time ranges that are required to reproduce observed abundances within errors.

Table D.1. Approximate time period (in years) during which the modeled abundance range matches the observed abundance range for B3.

B3	$n \times 10^7$			n 10^8			n 10^9		
	Fast	Medium	Slow	Fast	Medium	Slow	Fast	Medium	Slow
CH_3OH	22 250–22 300	86 000–87 000	420 000–430 000	22 700–22 800	88 000–89 000	439 000	23 200–23 300	91 000–91 500	445 000–450 000
C_2H_5OH	23 400–23 600	91 000–91 500	430 000–440 000	23 800–24 000	92 800–93 400	440 000	24 500–24 700	95 700–96 000	455 000
CH_3CHO	22 800–23 800	85 000–91 500	405 000–410 000	24 000–24 800	86 700–89 000★	415 000–420 000	23 200–29 000	96 000–97 500	43 5000★
CH_3OCHO	†	89 000★	365 000–375 000	21 600–21 900	90 000★	470 000–475 000★	>21 300	99 000–101 000★	485 000–495 000★
CH_3CN	>22 000	>84 000	>405 000	>22 500	>87 000	>417 000	>23 300	>89 700	>430 000
CH_2CHCN	>28 500	95 200–130 000	440 000–475 000	>29 000	97 600–141 000	470 000–485 000	>34 000	100 000–145 000	480 000–500 000
C_2H_5CN	†	97 500–98 500	475 000	†	>102 000	490 000	†	>103 000	500 000
HC_3N	21 600–21 800	84 000–84 500	400 000–405 000	22 100–22 300	86 000–87 000	418 000–420 000	22 700–23 000	89 000–89 600	430 000–435 000
Best time period fit	no fit	84 500–97 500	375 000–475 000	no fit	87 000–102 000	420 000–490 000	no fit	89 600–103 000	435 000–500 000
Temperatures (K)	95–158	93–116	78–120	96–164	98–133	96–127	105–223	104–134	102–132
Limiters	HC_3N-C_2H_3CN	HC_3N-C_2H_5CN	CH_3OCHO-C_2H_5CN	CH_3OCHO-CH_2CHCN	HC_3N-C_2H_5CN	HC_3N-C_2H_5CN	HC_3N-CH_2CHCN	HC_3N-C_2H_5CN	HC_3N-C_2H_5CN

Notes. The star symbol indicates that more than one time range fits the observed abundance. The dagger symbol indicates that the observed abundance is not reached by the model (too low).

Table D.2. As Table D.1 for B1/B2.

B1/B2	$n \times 10^7$			n 10^8			n 10^9		
	Fast	Medium	Slow	Fast	Medium	Slow	Fast	Medium	Slow
CH_3OH	>21 800	>85 000	>415 000	>22 200	>87 000	>425 000	>22 800	>89 000	>435 000
C_2H_5OH	>22 900	90 000–93 000	425 000–445 000	>23 300	91 000–95 000	435 000–450 000	24 000–26 000	93 800–97 500	440 000–465 000
CH_3CHO	21 700–23 800	81 500–91 300	330 000–410 000	23 000–24 800	83 000–95 000	405 000–425 000	22 600–29 000	94 500–97 500	460 000–480 000
CH_3OCHO	>25 000	75 500–78 500★	360 000–375 000	21 900–22 000★	90 000–90 600★	455 000–475 000★	21 000–21 500	91 000–92 000*	445 000★
CH_3CN	19 000–20 000	74 500–75 500	360 000–365 000	22 100–22 200	85 000–85500	407 000–410 000	22 600–22 900	87 600–88 000	418 000–420 000
CH_2CHCN	10^{-12}–10^{-11}	10^{-12}–10^{-11}	10^{-11}–10^{-10}	10^{-13}	10^{-12}	10^{-12}	10^{-14}–10^{-13}	6×10^{-14}–10^{-13}	8×10^{-13}–5×10^{-12}
C_2H_5CN	10^{-14}–10^{-12}	10^{-14}–5×10^{-13}	10^{-13}–10^{-12}	10^{-15}–10^{-14}	10^{-15}–10^{-14}	10^{-14}	10^{-17}–10^{-15}	7×10^{-16}	10^{-14}
HC_3N	20 000–21 800	79 500–84 000	365 000–405 000	21 000–22 300	82 400–86800	400 000–420 000	21 600–22 900	84 900–89 500	410 000–432 000
Best time period fit	20 000–25 000	75 500–90 000	365 000–425 000	22 000–23 300	85 500–91 000	410 000–455 000	21 500–24 000	88 000–94 500	420 000–460 000
Temperatures (K)	81–123	76–105	75–98	96–107	95–107	92–111	92–114	100–114	96–113
Limiters	CH_3CN-CH_3OCHO	CH_3CN-C_2H_5OH	CH_3CN-C_2H_5OH	CH_3OCHO-C_2H_5OH	CH_3CN-C_2H_5OH	CH_3CN-CH_3OCHO	CH_3OCHO-C_2H_5OH	CH_3CN-CH_3CHO	CH_3CN-CH_3CHO

Notes. Because vinyl and ethyl cyanide were not detected, the rows for CH_2CHCN and C_2H_5CN are the model abundances for the time period. The star symbol indicates that more than one time range fits the observed abundance.

Table D.3. As Table D.1 for A.

A	$n \times 10^7$			n 10^8			n 10^9		
	Fast	Medium	Slow	Fast	Medium	Slow	Fast	Medium	Slow
CH_3OH	21 700–22 300	84 000–87 000	415 000–430 000	22 000–22 800	86 500–89 000	423 000–438 000	22 700–23 200	88 500–92 000	438 000–460 000
C_2H_5OH	>23 000	90 000–96 200	430 000–440 000★	>23 500	92 000–96 500	439 000–452 000	>24 100	94 000–99 500	450 000–465 000
CH_3CHO	13 800–23 400	52 000–90 000	260 000–410 000	22 300–24 500	81 500–94 300	395 000–420 000	22 000–23 500	83 000–97 000	450 000–475 000
CH_3OCHO	>24 500	89 000–90 500★	350 000–365 000	21 700–22 100★	93 000–95 300★	460 000–465 000	20 500–21 000	91 000–92 000★	470 000–485 000★
CH_3CN	21 300–23 000	80 000–87 000	370 000–410 000	22 400–23 800	86 000–89 000	415 000–425 000	23 000–24 700	89 000–92 000	425 000–435 000
CH_2CHCN	>28 500	95 000–105 000	435 000–465 000	>28 500	97 500–110 000	470 000–480 000	>32 000	99 500–110 000	480 000–490 000
C_2H_5CN	>25 200	97 300–99 000	472 000–480 000	>29 000	>105 000	490 000	not reproduced	>10 3000	500 000
HC_3N	21 000–21 600	81 500–85 000	380 000–400 000	21 400–22 100	83 500–86 000	405 000–415 000	22 000–22 700	86 000–88 700	418 000–430 000
Best time period fit	21 600–28 500	85 000–97 300	365 000–472 000	22 100–28 500	86 000–105 000	415 000–490 000	no fit	88 700–103 000	430 000–500 000
Temperatures (K)	93–158	94–121	75–119	97–158	96–139	94–127	88–198	102–134	100–132
Limiters	HC_3N CH_2CHCN	HC_3N C_2H_5CN	CH_3OCHO C_2H_5CN	HC_3N C_2H_5CN	HC_3N C_2H_5CN	HC_3N C_2H_5CN	CH_3OCHO CH_2CHCN	HC_3N C_2H_5CN	HC_3N C_2H_5CN

Notes. The star symbol indicates that more than one time fits the observed abundance.

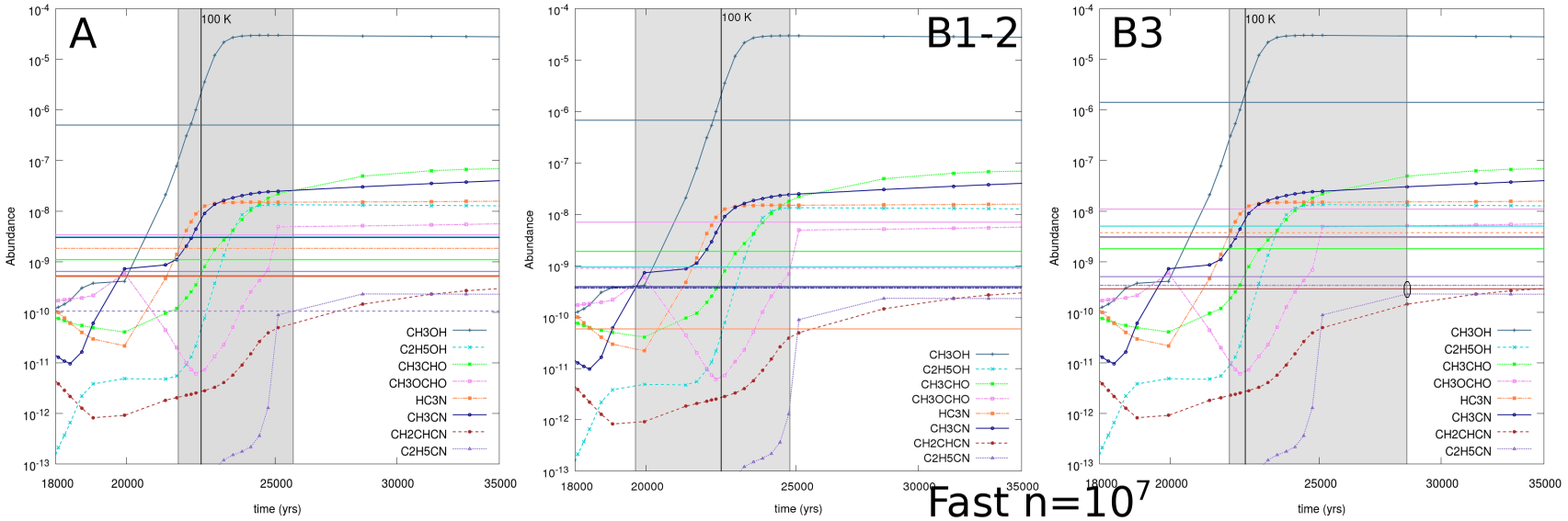

Fig. D.1. Abundances vs. H_2 for CH_3OH, C_2H_5OH, CH_3CHO, CH_3OCHO, HC_3N, CH_3CN, CH_2CHCN, and C_2H_5CN using IC 5 with a density of 10^7 cm^{-3} and a fast warm-up time of 50 kyr are shown for G35.20 A (*left*), B1/B2 (*middle*), and B3 (*right*). The time period shown is only a part of the modeled time, from 180 00 to 35 000 yr. The time range in which all abundances can be reproduced with an error of 1 order of magnitude are shaded in gray. The abundance of C_2H_5CN in B3 is not reproduced so a small black ellipse shows the gap between the lower abundance limit and the modeled abundance.

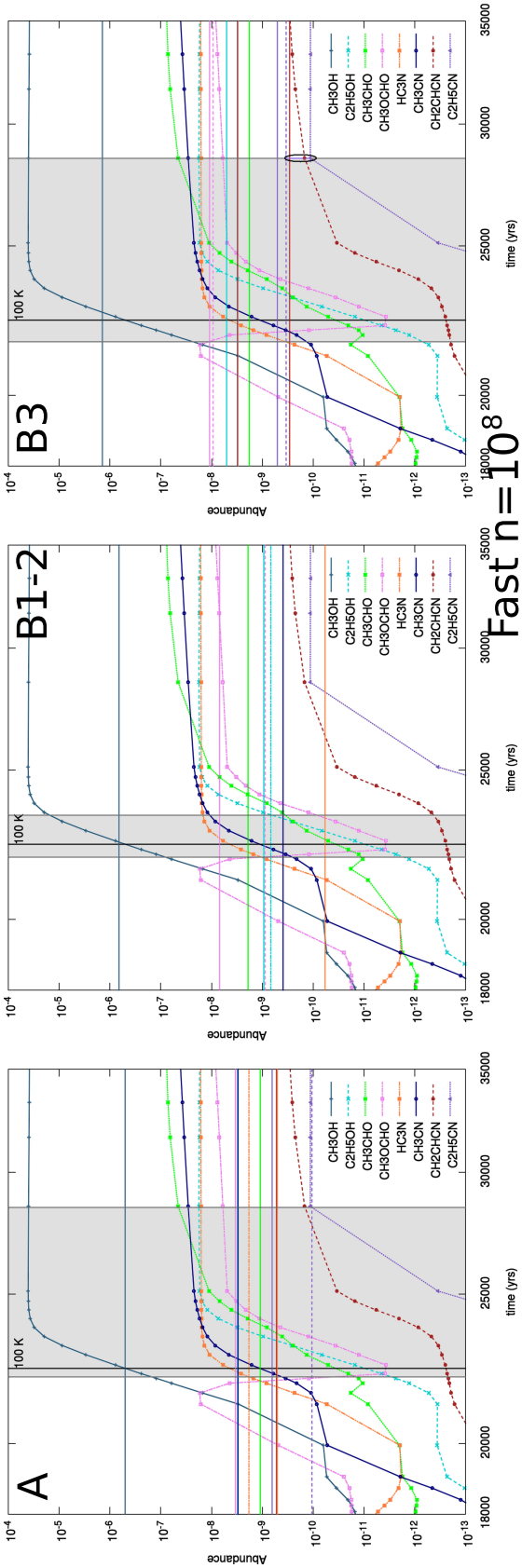

Fig. D.2. Abundances vs. H_2 for CH_3OH, C_2H_5OH, CH_3CHO, CH_3OCHO, HC_3N, CH_3CN, CH_2CHCN, and C_2H_5CN using IC 5 with a density of 10^8 cm^{-3} and a fast warm-up time of 50 kyr are shown for G35.20 A (*left*), B1/B2 (*middle*), and B3 (*right*). The time period shown is only a part of the modeled time, from 18 000 to 35 000 yr. The time range in which all abundances can be reproduced with an error of 1 order of magnitude are shaded in gray. The abundance of C_2H_5CN in B3 is not reproduced so a small black ellipse shows the gap between the lower abundance limit and the modeled abundance.

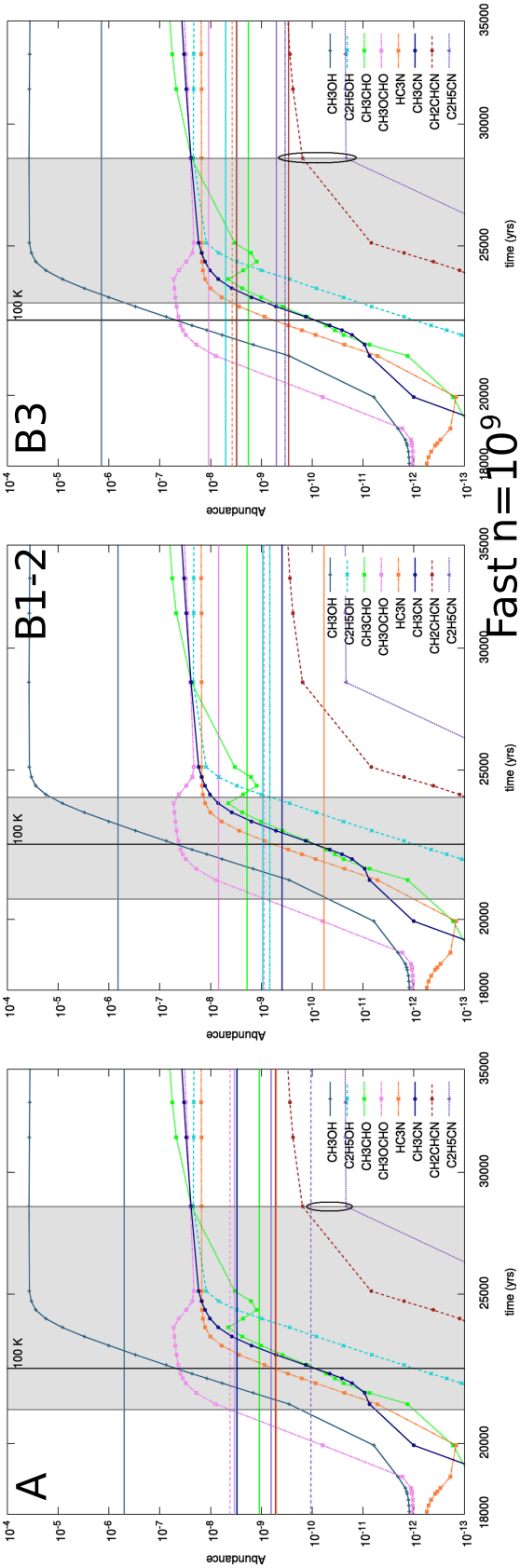

Fig. D.3. Abundances vs. H_2 for CH_3OH, C_2H_5OH, CH_3CHO, CH_3OCHO, HC_3N, CH_3CN, CH_2CHCN, and C_2H_5CN using IC 5 with a density of 10^9 cm^{-3} and a fast warm-up time of 50 kyr are shown for G35.20 A (*left*), B1/B2 (*middle*), and B3 (*right*). The time period shown is only a part of the modeled time, from 18 000 to 35 000 yr. The time range in which all abundances can be reproduced with an error of 1 order of magnitude are shaded in gray. The abundance of C_2H_5CN in A and B3 is not reproduced so a small black ellipse shows the gap between the lower abundance limit and the modeled abundance.

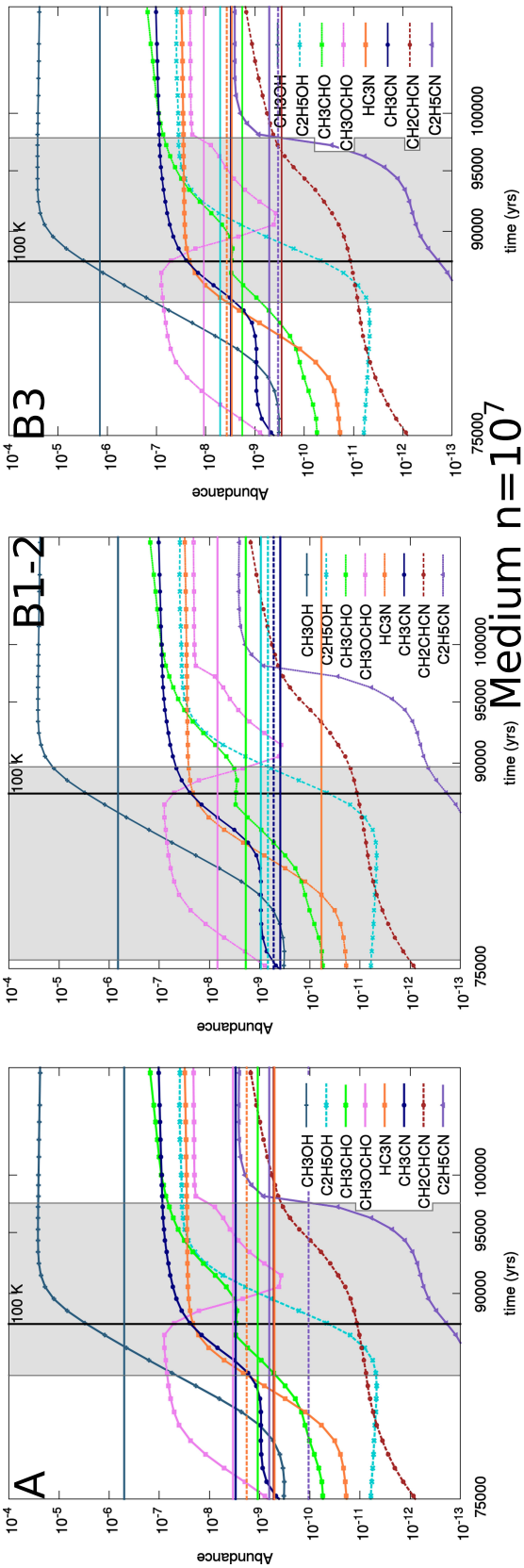

Fig. D.4. Abundances vs. H_2 for CH_3OH, C_2H_5OH, CH_3CHO, CH_3OCHO, HC_3N, CH_3CN, CH_2CHCN, and C_2H_5CN using IC 5 with a density of 10^7 cm^{-3} and a medium warm-up time of 200 kyr are shown for G35.20 A (*left*), B1/B2 (*middle*), and B3 (*right*). The time period shown is only a part of the modeled time, from 70 to 120 kyr for A and B3 and 30–105 kyr for B1/B2. The time range in which all abundances can be reproduced with an error of 1 order of magnitude are shaded in gray.

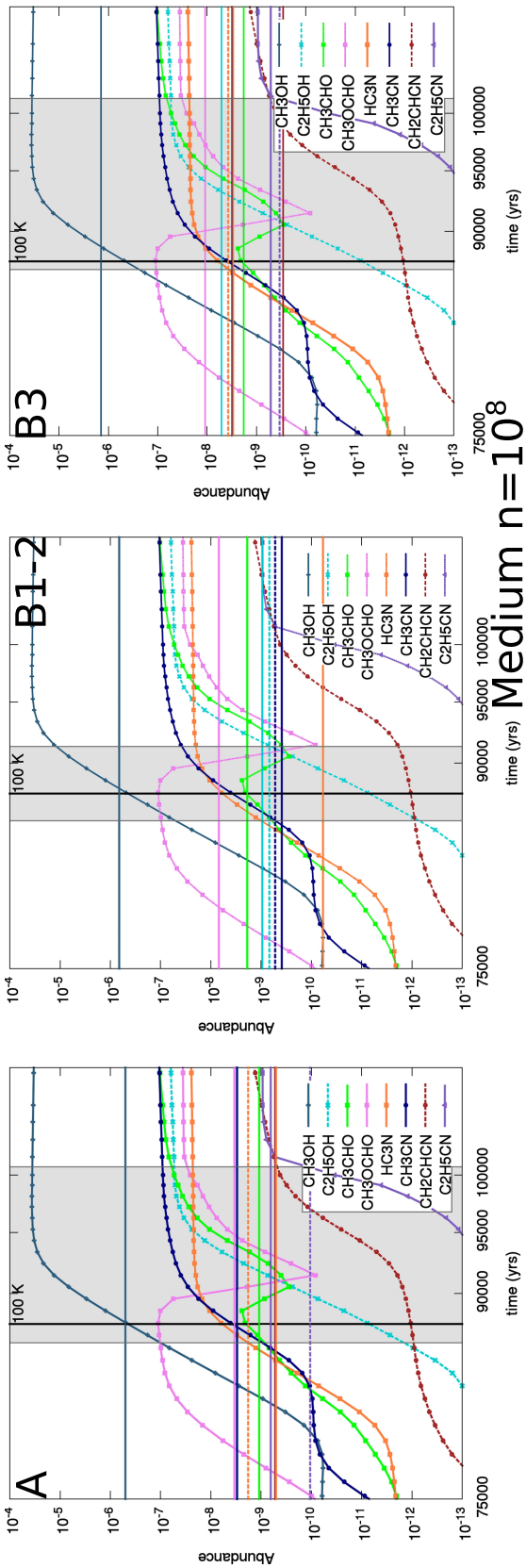

Fig. D.5. Abundances vs. H_2 for CH_3OH, C_2H_5OH, CH_3CHO, CH_3OCHO, HC_3N, CH_3CN, CH_2CHCN, and C_2H_5CN using IC 5 with a density of 10^8 cm^{-3} and a medium warm-up time of 200 kyr are shown for G35.20 A (*left*), B1/B2 (*middle*), and B3 (*right*). The time period shown is only a part of the modeled time, from 70 to 120 kyr for A and B3 and 30–105 kyr for B1/B2. The time range in which all abundances can be reproduced with an error of 1 order of magnitude are shaded in gray. The abundance of C_2H_5CN in B3 is not reproduced.

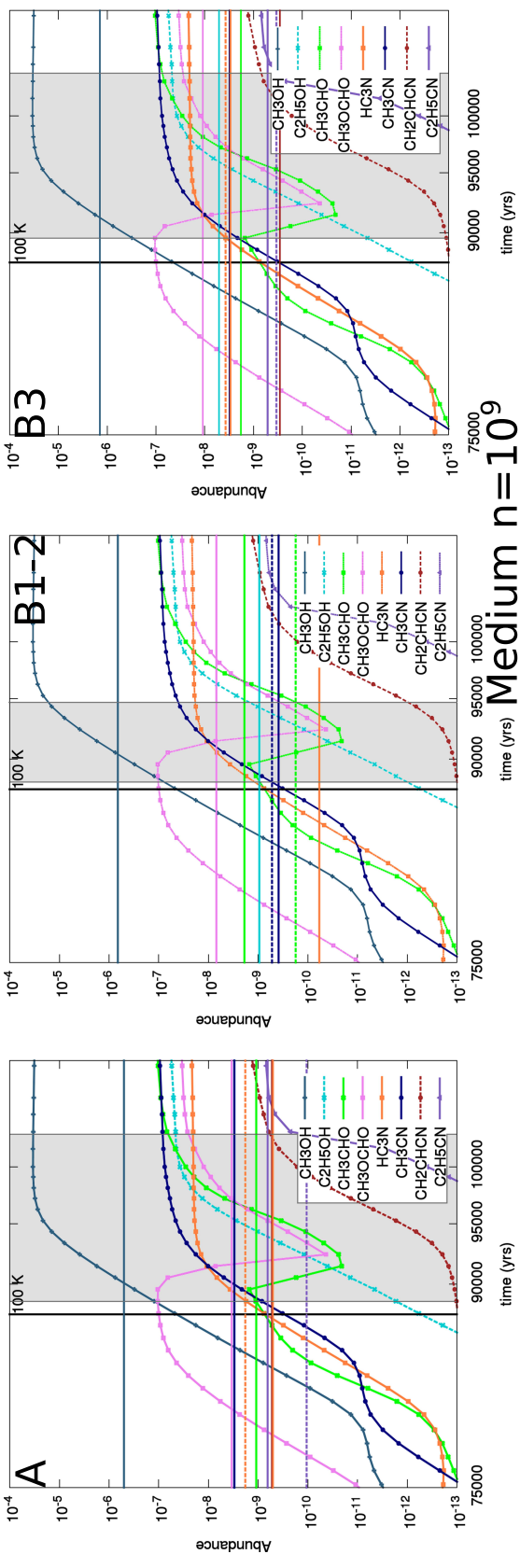

Fig. D.6. Abundances vs. H_2 for CH_3OH, C_2H_5OH, CH_3CHO, CH_3OCHO, HC_3N, CH_3CN, CH_2CHCN, and C_2H_5CN using IC 5 with a density of 10^9 cm^{-3} and a medium warm-up time of 200 kyr are shown for G35.20 A (*left*), B1/B2 (*middle*), and B3 (*right*). The time period shown is only a part of the modeled time, from 70 to 120 kyr for A and B3 and 30–105 kyr for B1/B2. The time range in which all abundances can be reproduced with an error of 1 order of magnitude are shaded in gray. The abundance of C_2H_5CN in B3 is not reproduced.

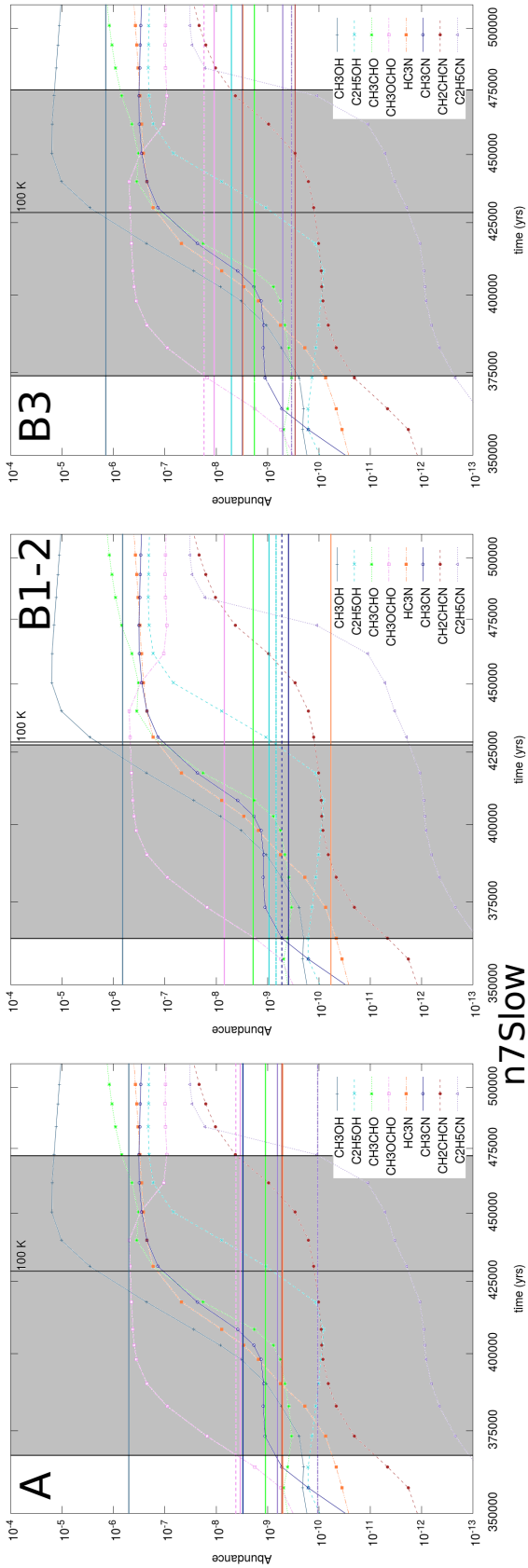

Fig. D.7. Abundances vs. H_2 for CH_3OH, C_2H_5OH, CH_3CHO, CH_3OCHO, HC_3N, CH_3CN, CH_2CHCN, and C_2H_5CN using IC 5 with a density of 10^7 cm^{-3} and a slow warm-up time of 1 Myr are shown for G35.20 A (*left*), B1/B2 (*middle*), and B3 (*right*). The time period shown is only a part of the modeled time, from 350 to 510 kyr. The time range in which all abundances can be reproduced with an error of 1 order of magnitude are shaded in gray.

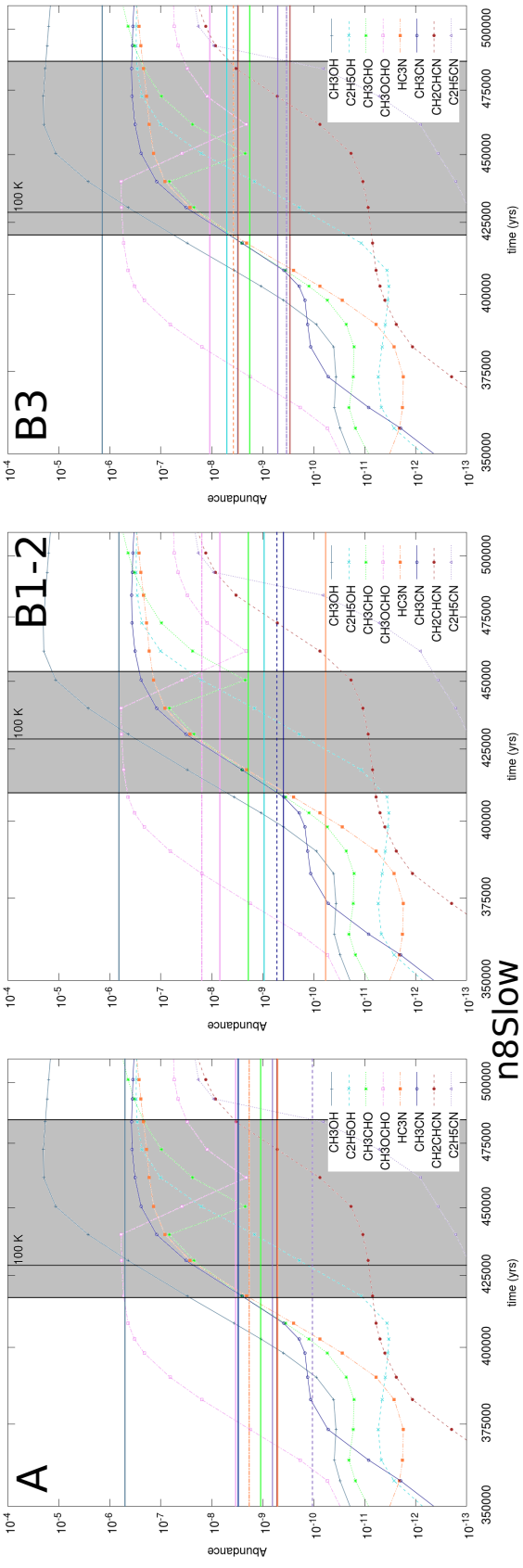

Fig. D.8. Abundances vs. H_2 for CH_3OH, C_2H_5OH, CH_3CHO, CH_3OCHO, HC_3N, CH_3CN, CH_2CHCN, and C_2H_5CN using IC 5 with a density of 10^7 cm^{-3} and a slow warm-up time of 1 Myr are shown for G35.20 A (*left*), B1/B2 (*middle*), and B3 (*right*). The time period shown is only a part of the modeled time, from 350 to 510 kyr. The time range in which all abundances can be reproduced with an error of 1 order of magnitude are shaded in gray.

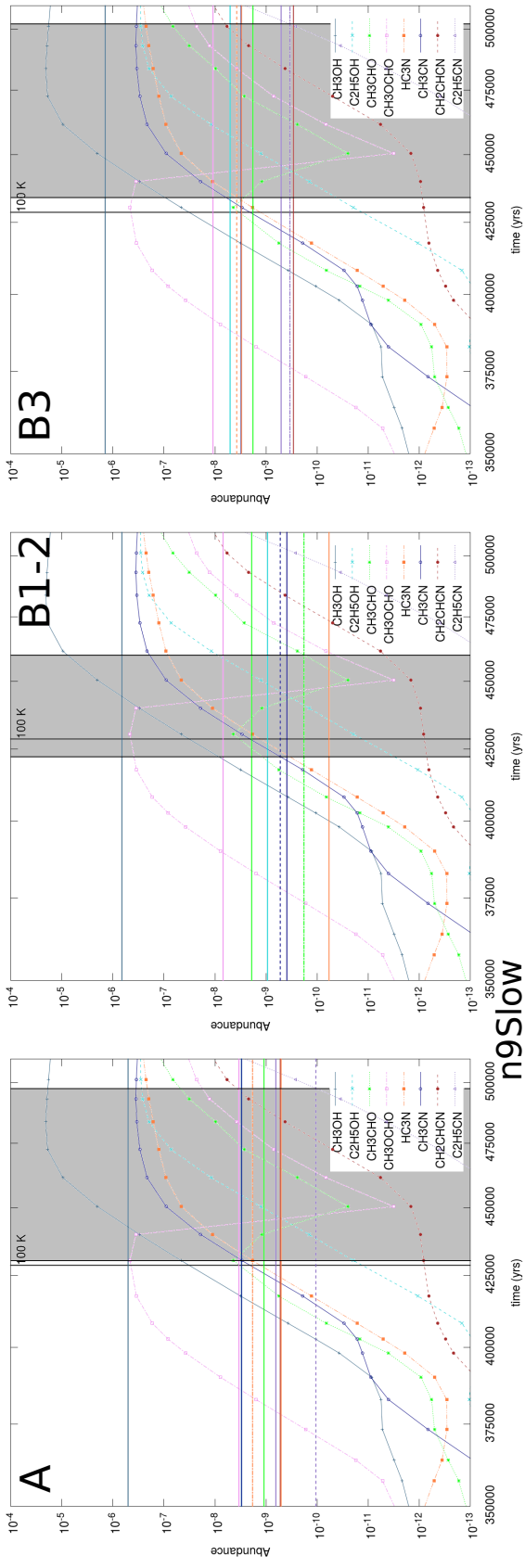

Fig. D.9. Abundances vs. H_2 for CH_3OH, C_2H_5OH, CH_3CHO, CH_3OCHO, HC_3N, CH_3CN, CH_2CHCN, and C_2H_5CN using IC 5 with a density of 10^9 cm^{-3} and a slow warm-up time of 1 Myr are shown for G35.20 A (*left*), B1/B2 (*middle*), and B3 (*right*). The time period shown is only a part of the modeled time, from 350 to 510 kyr. The time range in which all abundances can be reproduced with an error of 1 order of magnitude are shaded in gray.